

Photonic Exponential Approximation via Cascaded TFLN Microring Resonators toward Softmax

Hyoseok Park¹ and Yeonsang Park^{1,*}

¹*Department of Physics, Chungnam National University, Daejeon 34134, Republic of Korea*

(Dated: March 16, 2026)

The rapid growth of large-scale AI models has intensified energy consumption and data-movement challenges in modern datacenters [1–3]. Photonic accelerators offer a promising path by executing the linear matrix multiplications of transformer inference at high throughput and low energy [4–8]. However, the softmax attention layer—which requires element-wise exponentiation followed by normalization—still relies on electronic post-processing [9–13], creating an electro-optic conversion bottleneck that negates much of the potential photonic advantage.

We present a cascaded micro-ring resonator (MRR) architecture that synthesizes the per-channel exponential function required by softmax, $e^{x_n - \max(x)}$, over a finite interval with tunable worst-case relative error. A control signal detunes each ring via an electro-optic mechanism; a weak probe at fixed frequency experiences Lorentzian transmission, and cascading N identical stages yields a multiplicative transfer function whose logarithm is approximately linear.

We derive mapping rules, depth-scaling estimates, and a minimax fitting formulation, and validate the framework with three-dimensional FDTD simulations of X-cut thin-film lithium niobate (TFLN) add-drop micro-ring resonators. Direct multi-ring FDTD validation extends to a five-ring cascade and confirms agreement with theory primarily over the upper operating range; deeper cascades and higher quality factors are assessed analytically. The cascade implements the per-channel exponential block—the key missing nonlinearity for photonic softmax; completing a full softmax additionally requires summation and normalization, which we discuss but do not implement here.

I. INTRODUCTION

Transformer inference is often limited by power and memory traffic, motivating optical accelerators that exploit parallel propagation and multiplexing [1, 2, 4, 5, 7, 9]. Recent perspective articles also discuss data-center power consumption as one motivation for optical computing [3, 8]. While linear operators are comparatively amenable to photonic implementation [4–6], the softmax function used in attention layers requires an exponential mapping together with global normalization—both difficult to realize in passive photonic circuits, where transmission is fundamentally bounded by unity. Parallel digital-hardware studies treat the exponential/softmax stage as a bottleneck and propose dedicated approximations [11–19]. Many integrated-photonic classifier demonstrations still rely on electronic post-processing for the final nonlinear readout [10]; the resulting electro-optic conversion overhead can negate the throughput and energy benefits of the photonic front-end. Here we address the exponential block specifically: we show that a passive Lorentzian cascade can be tuned so that its logarithm is approximately linear over a finite interval, enabling exponential-function synthesis with explicit depth scaling while remaining compatible with integrated microring platforms [20–24]. We term this cascade block an *approximate exponential function* (AEF) unit. Completing a full softmax additionally requires summation and reciprocal normalization, which we discuss but do not implement here.

We extend the theoretical framework with three-dimensional FDTD simulations of a single X-cut TFLN add-drop micro-ring resonator. The simulated device parameters—quality factor, free spectral range, and electro-optic sensitivity—calibrate the cascade design parameters, bridging analytical fitting and physically realizable hardware. Two operating regimes emerge from this calibration: an FDTD-characterized regime with moderate drop-port depth ($D_{\max} \approx 0.36$), where the analytic error stays below $\sim 5\%$ for $N \leq 7$ but the power budget limits practical cascades to $N \leq 5$; and a projected high- Q regime ($D_{\max} \geq 0.95$), enabling deeper cascades ($N \leq 30$) with sub-percent error. Cascade performance is predicted analytically and validated by a five-ring cascade 3D FDTD simulation (Sec. IV).

The paper is organized as follows: Section II presents the mapping, transfer model, and depth-design rules; Section III provides numerical fits and validation; Section IV describes the single-ring TFLN device design and FDTD validation; Section V assesses physical feasibility including voltage requirements, insertion loss, and energy efficiency; Section VI discusses implementation scope, platform comparisons, and limits; and Section VII concludes.

II. MODEL AND DESIGN FRAMEWORK

Target mapping. Let $x = (x_1, \dots, x_K) \in \mathbb{R}^K$ be an arbitrary real-valued sequence (or vector). Directly generating $\exp(x_n)$ as a *passive* optical transmission is impossible in general because $\exp(x)$ grows beyond unity while a passive transmission satisfies $0 < T \leq 1$ [25]. However, for softmax,

* yeonsang.park@cnu.ac.kr; Corresponding author

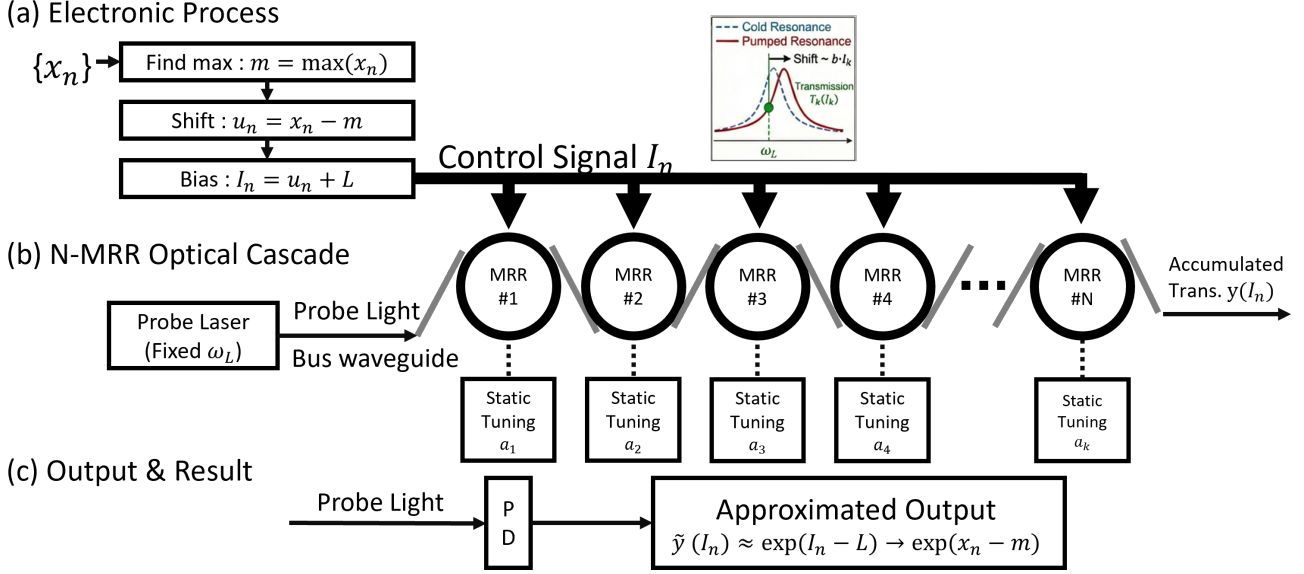


FIG. 1: Overview of the control–probe add-drop cascade N -MRR exponential block. (a) Electronic preprocessing maps an arbitrary input sequence $\{x_n\}$ to a nonnegative control signal via $m = \max_n x_n$, $u_n = x_n - m$, and $I_n = u_n + L$ with $L = m - \min_n x_n$. (b) The control signal I_n induces resonance shifts in a cascade of N rings, while a weak fixed-frequency probe propagates through the serial add-drop cascade (the drop output of each ring feeds the next stage), experiencing multiplicative transmission. (c) After photodetection, the block implements $y(I_n) \approx \exp(I_n - L) \approx \exp(x_n - m)$, i.e., the normalized exponential used in softmax.

$$\text{softmax}(x)_n = \frac{e^{x_n}}{\sum_j e^{x_j}}, \quad (1)$$

a common shift cancels:

$$\frac{e^{x_n+c}}{\sum_j e^{x_j+c}} = \frac{e^{x_n}}{\sum_j e^{x_j}} \quad (\forall c \in \mathbb{R}). \quad (2)$$

Thus it suffices to generate

$$e^{x_n-m}, \quad m \equiv \max_j x_j, \quad (3)$$

since the global factor e^m cancels.

To ensure a nonnegative control-signal amplitude, define

$$u_n \equiv x_n - m \leq 0, \quad L \equiv -\min_n u_n = m - \min_n x_n \geq 0, \quad (4)$$

and map each scalar to a nonnegative control-signal amplitude

$$I_n \equiv u_n + L \in [0, L]. \quad (5)$$

Then

$$e^{x_n-m} = e^{u_n} = e^{I_n-L}. \quad (6)$$

Hence the optical design task is to realize, for $I \in [0, L]$,

$$f(I) = e^{I-L} \in [e^{-L}, 1]. \quad (7)$$

Control–probe transfer. Consider a weak probe at fixed angular frequency ω_L . For the k th ring, let $\omega_{0,k}$ denote its resonance frequency and $\Gamma > 0$ its loaded half-width at half maximum (HWHM). Define the detuning

$$\Delta\omega_k \equiv \omega_L - \omega_{0,k}. \quad (8)$$

Near resonance, the normalized Lorentzian transmission is modeled as [20, 21]

$$T_k(\Delta\omega_k) = \frac{1}{1 + \left(\frac{\Delta\omega_k}{\Gamma}\right)^2}. \quad (9)$$

In a control–probe architecture, a nonnegative control-signal amplitude $I \geq 0$ shifts the ring resonance. Here I denotes a generic control amplitude: for optical-pump operation it maps to optical intensity, while for EO operation it maps to electrical control level (e.g., voltage). Across many physical mechanisms (optical pump via Kerr/XPM, EO drive via Pockels effect, thermal, carrier tuning), the shift can be linearized on a working range [20, 26–30]:

$$\omega_{0,k}(I) = \omega_{0,k}^{(0)} + \eta I, \quad (10)$$

where $\omega_{0,k}^{(0)}$ is the cold-cavity resonance and η is the control-to-resonance sensitivity. In practice, the control channel can be optical or electrical (optical pump, EO/Pockels drive, thermal, or carrier tuning); a quantitative EO feasibility example is given in the Discussion. With $\Delta\omega_{0,k} \equiv \omega_L - \omega_{0,k}^{(0)}$, the control-dependent detuning becomes

$$\Delta\omega_k(I) = \Delta\omega_{0,k} - \eta I. \quad (11)$$

Define dimensionless parameters

$$a_k \equiv \frac{\Delta\omega_{0,k}}{\Gamma}, \quad b \equiv -\frac{\eta}{\Gamma}. \quad (12)$$

Then Eq. (9) yields the control-to-probe transfer of a single ring,

$$T_k(I) = \frac{1}{1 + (a_k + bI)^2}. \quad (13)$$

Physical meaning: a_k is a *static detuning* in linewidth units (set by heater/carrier tuning/fabrication), and $|b|$ is the *normalized sensitivity magnitude* (linewidths of resonance shift per unit control-signal amplitude); the sign convention is absorbed into the detuning expression. For “same-material/same-geometry” rings, b is often common, while a_k can be tuned per ring.

Sign convention. Simultaneously flipping $(a_k, b) \mapsto (-a_k, -b)$ leaves $T_k(I)$ unchanged, so we may take $b > 0$ without loss of generality.

Let N rings be cascaded in a serial add-drop topology: $T_k(I)$ denotes the add-to-drop transmission of ring k , and the drop output of ring k feeds the add (input bus) port of ring $k+1$. Assuming the probe is sufficiently weak so the control channel dominates the resonance shift, the normalized probe output is the product

$$y(I) \equiv \frac{P_{\text{out}}^{(\text{probe})}(I)}{P_{\text{in}}^{(\text{probe})}} = \prod_{k=1}^N T_k(I) = \prod_{k=1}^N \frac{1}{1 + (a_k + bI)^2}. \quad (14)$$

To focus on the *shape* of the approximation, we allow a global scale factor $C > 0$:

$$\tilde{y}(I) \equiv C y(I). \quad (15)$$

In softmax, $p_n = C e^{I_n - L} / \sum_j C e^{I_j - L}$, so C cancels between numerator and denominator and is physically inessential; nevertheless it is convenient for error analysis. For a fixed $(N, b, \{a_k\})$, the optimal C for the minimax log-error in Eq. (18) can be written in closed form. Let $g(I) \equiv \ln y(I) - (I - L)$ on $[0, L]$. Then the minimax-optimal shift is $\ln C^* = -(\max_I g(I) + \min_I g(I))/2$, yielding $E_\infty = (\max_I g(I) - \min_I g(I))/2$.

Taking logarithms,

$$\ln \tilde{y}(I) = \ln C - \sum_{k=1}^N \ln(1 + (a_k + bI)^2). \quad (16)$$

The target $\ln f(I) = I - L$ is linear; hence exponential approximation is equivalent to the *log-linearization* goal

$$\ln \tilde{y}(I) \approx I - L \quad \text{uniformly on } I \in [0, L]. \quad (17)$$

Error metric. Define the worst-case *log-error* on $[0, L]$:

$$E_\infty \equiv \sup_{I \in [0, L]} \left| \ln \tilde{y}(I) - (I - L) \right|. \quad (18)$$

If $E_\infty \leq \varepsilon_{\log}$, then for all $I \in [0, L]$,

$$e^{-\varepsilon_{\log}} \leq \frac{\tilde{y}(I)}{f(I)} \leq e^{\varepsilon_{\log}} \Rightarrow \left| \frac{\tilde{y}(I)}{f(I)} - 1 \right| \leq e^{\varepsilon_{\log}} - 1. \quad (19)$$

Thus achieving a prescribed worst-case relative error ε is guaranteed by

$$E_\infty \leq \varepsilon_{\log} \equiv \ln(1 + \varepsilon) \approx \varepsilon. \quad (20)$$

Depth scaling. We derive depth-related constraints and design rules for a prescribed approximation tolerance.

Necessary slope condition. Differentiate Eq. (16):

$$\frac{d}{dI} \ln y(I) = - \sum_{k=1}^N \frac{2b(a_k + bI)}{1 + (a_k + bI)^2}. \quad (21)$$

Since $|2u/(1 + u^2)| \leq 1$ for all real u ,

$$\left| \frac{d}{dI} \ln y(I) \right| \leq N|b|. \quad (22)$$

The target $\ln f(I) = I - L$ has constant slope $+1$, so a necessary condition to track it is

$$N|b| \gtrsim 1. \quad (23)$$

Near-optimal parameterization. The full design problem can be written as a minimax fit in the log domain [31]:

$$\min_{a_1, \dots, a_N, \ln C} \sup_{I \in [0, L]} |r(I)|, \quad (24)$$

$$r(I) \equiv \ln C - \sum_{k=1}^N \ln(1 + (a_k + bI)^2) - (I - L).$$

This objective is permutation-invariant in the a_k 's (ring index k). In practice (and in numerical experiments

reported below), the optimizer frequently collapses to a permutation-symmetric solution

$$a_1 = \dots = a_N \equiv a, \quad (25)$$

reducing the design to two parameters (a, b) (plus C). With Eq. (25),

$$\tilde{y}(I) = C y(I) = C \left[\frac{1}{1 + (a + bI)^2} \right]^N. \quad (26)$$

A robust initialization is obtained by placing the midpoint of the interval on the Lorentzian half-maximum flank and matching the slope:

$$a + b\frac{L}{2} \approx -1, \quad Nb \approx 1. \quad (27)$$

These two equations already yield a good design; a small (two-parameter) refinement can then enforce the desired worst-case tolerance.

Local expansion and depth scaling. A Taylor expansion of the log-domain residual around the flank-centered point $I_0 = L/2$ (with $a + bI_0 = -1$ and $Nb = 1$) shows that the quadratic term vanishes identically, leaving a leading cubic residual $r(\delta) \sim \delta^3/(6N^2)$. Over $I \in [0, L]$, this implies $E_\infty \sim L^3/N^2$, so that achieving a prescribed tolerance ε_{\log} requires $N \propto L^{3/2}/\sqrt{\varepsilon_{\log}}$, which explains the scaling used in Eq. (28). The full derivation is provided in Supplementary Sec. S0; an intuitive local-expansion summary appears in Sec. S1.

Practical engineering estimate. Given L and a target worst-case relative error ε , define $\varepsilon_{\log} = \ln(1 + \varepsilon)$. A heuristic engineering estimate (not a rigorous bound) that matched our percent-level numerical designs is

$$N \approx \left\lceil \max \left(\frac{1}{b_{\max}}, \kappa \frac{L^{3/2}}{\sqrt{\varepsilon_{\log}}} \right) \right\rceil, \quad (28)$$

where b_{\max} is the physically achievable sensitivity bound and $\kappa \simeq 0.07$ for the identical-detuning flank design with a minimax refinement. After choosing N , set $b = \min(b_{\max}, 1/N)$ and $a = -1 - bL/2$ as initialization, then refine (a, b) by a two-parameter minimax fit on $[0, L]$.

A heuristic conservative screening bound $N \geq \lceil (L^2/4 + 1/(2b^2))/\ln(1 + \varepsilon) \rceil$ (derived via the same local-expansion argument; see Supplementary Sec. S1) provides a quick upper estimate but is not a rigorous guarantee.

III. NUMERICAL FITS AND VALIDATION

We validate the analytical framework with minimax numerical fits and sampled robustness checks. Figure 2 shows the fitted approximation quality at $L = 8$: the

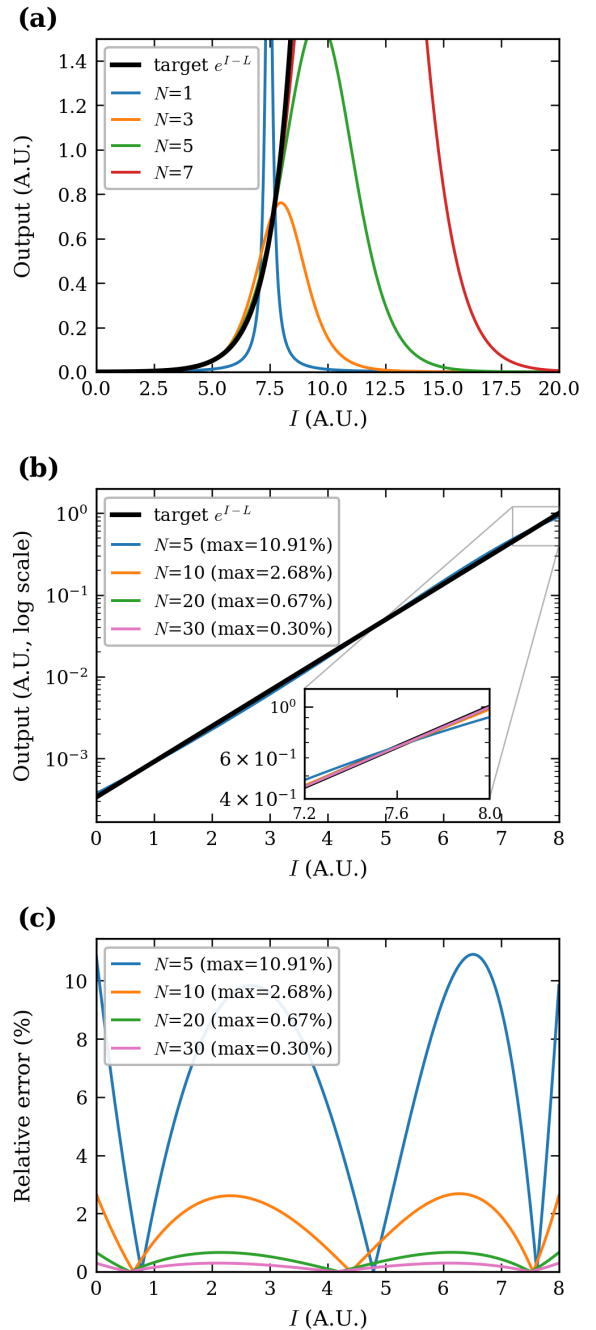


FIG. 2: Minimax cascade fits at $L = 8$. (a) Linear scale: shallow cascades ($N = 1, 3, 5, 7$) over $I \in [0, 20]$. The target e^{I-L} (black) is progressively better matched as N increases. (b) Log scale: depth comparison ($N = 5, 10, 20, 30$) on $I \in [0, 8]$. Inset zooms into $I \in [6, 8]$ showing convergence. (c) Pointwise relative error showing the Chebyshev equioscillation pattern characteristic of minimax optimality.

top (linear) panel plots $N = 1, 3, 5, 7$ over $I \in [0, 20]$, the middle (log) panel compares $N = 5, 10, 20, 30$ on $I \in [0, 8]$, and the bottom panel shows the pointwise relative error

TABLE I: Depth comparison for $L = 8$ using fitted $\tilde{y}(I) = C[1 + (a + bI)^2]^{-N}$ (same fitting pipeline for all N).

N	a	b	max rel. err.	mean rel. err.
5	-2.0789	0.21658	10.9%	6.43%
10	-1.4588	0.10202	2.68%	1.65%
20	-1.2135	0.05025	0.67%	0.42%
30	-1.1392	0.03341	0.30%	0.19%

with the characteristic Chebyshev equioscillation pattern.

We fit identical-detuning cascades (Eq. 25) on $I \in [0, L]$ and compare several depths using a minimax criterion.

Table I makes the accuracy–depth trade-off explicit at $L = 8$. A worked input-to-output example demonstrating the mapping from an arbitrary input sequence $x = [-3.2, 1.2, 4.8, -0.9]$ through the cascade is provided in Supplementary Sec. S2. The example shows that the $N = 10$ cascade keeps the worst-case relative error below 2.7% across all channels.

Empirical calibration. We calibrate the effective logit range L_{eff} from autoregressive Transformers (distilgpt2/gpt2) [1, 32–35] at context length 128, finding $L_{\text{eff},0.999} \approx 7$ –9 at the 50th–90th percentiles (Supplementary Sec. S2). A clipping threshold $t^* = -12$ preserves p99 softmax accuracy below 0.1%. Full protocol details, clipping-sweep tables/plots, and per-run statistics are provided in Supplementary Sec. S3.

A synthetic design-space map (Supplementary Table S3) shows that near $L \approx 8$, moderate depth ($N \geq 10$) reaches few-percent error, whereas $L \gtrsim 12$ requires deeper cascades. All fits follow the same pipeline: minimize the worst-case log-error on a uniform grid, initialize from the flank rules in Eq. (27), perform multi-start global search, and apply bounded local refinement; implementation details and scripts are provided in a public repository [36] (commit: 585e695).

IV. TFLN SINGLE-RING DEVICE DESIGN AND FDTD VALIDATION

A. Waveguide and ring geometry

The device is based on an X-cut thin-film lithium niobate (LiNbO₃) on insulator wafer with a 600 nm-thick LiNbO₃ film on SiO₂. A 500 nm-deep rib etch defines a 1.4 μm -wide single-mode waveguide with a 100 nm unetched slab (Fig. 3). Lumerical MODE simulations yield $n_{\text{eff}} = 1.903$ and $n_g = 2.24$ at $\lambda = 1550$ nm for the fundamental TE₀ mode.

The ring resonator ($R = 20 \mu\text{m}$, $L_{\text{ring}} = 125.7 \mu\text{m}$) is configured as an add-drop resonator with 100 nm coupling gaps (Fig. 4). The FDTD-measured free spectral range is $\text{FSR} = 8.29$ nm ($n_g \approx 2.30$), slightly above the MODE value due to bend-induced dispersion.

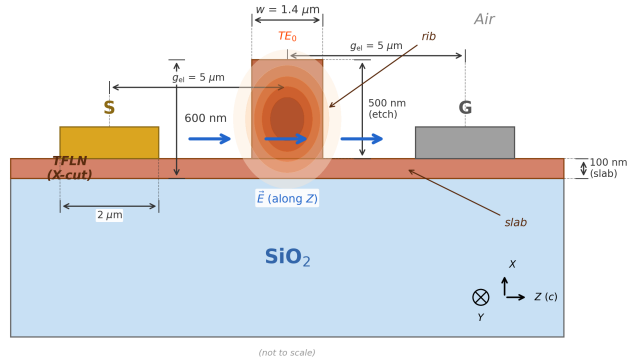


FIG. 3: Cross-section of the X-cut TFLN rib waveguide on a SiO₂ substrate. The 600 nm LiNbO₃ film is etched 500 nm to form a 1.4 μm -wide single-mode rib waveguide. Lateral signal (S) and ground (G) electrode positions are indicated; electrode design details are discussed in Sec. IV D.

Table II summarizes the waveguide and ring parameters.

TABLE II: Waveguide and ring parameters of the X-cut TFLN micro-ring resonator. Electro-optic electrode parameters are listed separately in Table III.

Parameter	Symbol	Value	Unit
Total TFLN thickness	t_{TFLN}	600	nm
Etch depth	t_{etch}	500	nm
Slab thickness	t_{slab}	100	nm
Waveguide width	w	1.4	μm
Bend radius	R	20	μm
Coupling gap	g	100	nm
Circumference	L_{ring}	125.7	μm
Free spectral range	FSR	8.29	nm
Effective index (TE ₀)	n_{eff}	1.903	—
Group index (TE ₀)	n_g	2.24	—
Extraordinary index	n_e	2.138	—

B. 3D FDTD Methodology

The ring resonator response is simulated using Lumerical 3D FDTD with conformal variant 1 meshing. A broadband TE₀ mode source (1530 nm to 1570 nm) is injected into the input bus waveguide, and through- and drop-port spectra are recorded. A “z-refined 3-fix” meshing strategy ensures convergence in the thin-film geometry [37]; detailed simulation setup is provided in Supplementary Sec. S4 (Table S6).

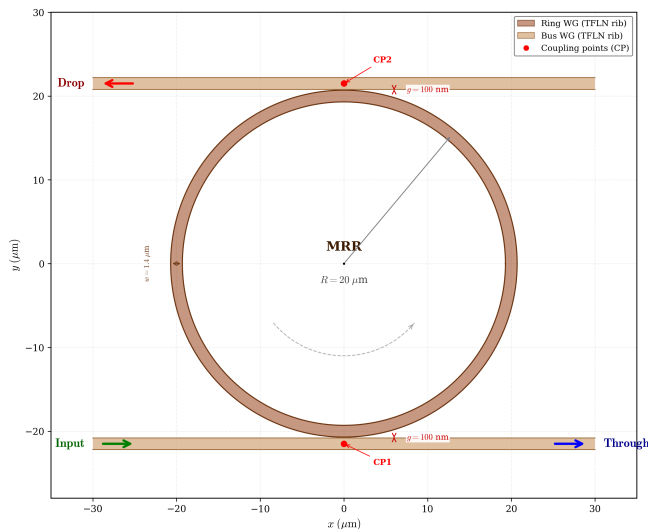


FIG. 4: Top view of the single add-drop micro-ring resonator used in the 3D FDTD simulation. The ring waveguide ($R = 20 \mu\text{m}$, $w = 1.4 \mu\text{m}$) is evanescently coupled to input and drop bus waveguides through 100 nm gaps at coupling points CP1 and CP2.

C. Single-Ring Add-Drop Results

Figure 5 shows the through- and drop-port spectra from 3D FDTD. Five resonances are resolved across 1530 nm to 1570 nm with $\text{FSR} = 8.29 \text{ nm}$ ($n_g \approx 2.30$).

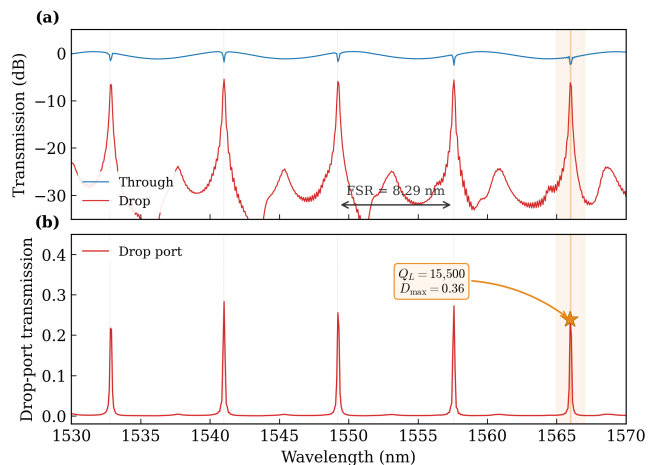


FIG. 5: Simulated through-port (blue) and drop-port (red) transmission spectra of the single add-drop micro-ring resonator from 3D FDTD. Top: logarithmic scale; bottom: linear scale. Five resonances are visible with $\text{FSR} \approx 8.29 \text{ nm}$.

Lorentzian fitting of the drop-port peaks yields $Q_L = 10,300\text{--}15,500$, with the best resonance at $\lambda = 1566 \text{ nm}$ reaching $Q_L = 15,500$ ($\text{FWHM} = 101 \text{ pm}$, $D_{\text{max}} = 0.360$, -4.4 dB). The through-port extinction ratio is 1.6 dB to

2.6 dB, and the five-resonance mean is $Q_L = 12,500 \pm 1,800$ ($D_{\text{max}} = 0.29\text{--}0.36$). CMT analysis of the best resonance gives $Q_i = Q_L / (1 - \sqrt{D_{\text{max}}}) = 15,500 / 0.400 \approx 38,800$, confirming that the 500 nm etch provides sufficient confinement and that the 100 nm gap places the ring in the coupling-limited regime. The cascade analysis below adopts the best-case FDTD calibration ($Q_L = 15,500$, $D_{\text{max}} = 0.360$); using the five-resonance mean would increase required voltages by $\sim 24\%$ (see Table IV caption).

The simulation time of 50 ps exceeds the loaded photon lifetime $\tau_L = Q_L \lambda_0 / (2\pi c) \approx 12.7 \text{ ps}$ by $\sim 4\times$, but the intrinsic lifetime $\tau_i \approx 32 \text{ ps}$ is comparable, so the extracted Q_i may be slightly conservative. An independent eigenmode (FDE) analysis of the same cross-section at $R = 20 \mu\text{m}$ —using a 300×300 mesh ($\Delta y \approx 10 \text{ nm}$, $5\times$ finer than the FDTD vertical grid)—yields $Q_{\text{rad+leak}} = 2.4 \times 10^7$; including bulk LiNbO_3 absorption ($\Gamma = 0.89$) gives a theoretical $Q_i > 10^7$ [37–42], confirming that the gap between the numerical Q_i and published values ($> 10^6$) originates from mesh discretization (Supplementary S4.5, Table S8). In the CMT framework, $D_{\text{max}} = [2\kappa / (2\kappa + \gamma)]^2$ increases as Q_i rises; at the present coupling gap, increasing Q_i to 10^6 would raise D_{max} from 0.36 to ~ 0.95 and Q_L from 15,500 to $\sim 25,200$.

Figure 6(a) shows a Lorentzian fit to the best drop-port resonance at $\lambda = 1566 \text{ nm}$, validating the cascade model (Eq. 9). Figure 6(b) demonstrates that cascading N copies of this FDTD-extracted Lorentzian reproduces the target exponential e^{I-L} with increasing fidelity as N grows.

To validate the cascade prediction directly, we performed a five-ring cascade 3D FDTD simulation using Tidy3D [43], a GPU-accelerated Maxwell solver. Five identical add-drop rings ($R = 20 \mu\text{m}$, $g = 100 \text{ nm}$) are connected through diagonal bus waveguides in a zigzag topology matching the single-ring design. The resulting $|E|^2$ field at $\lambda = 1549 \text{ nm}$ [Fig. 6(d)] confirms resonant excitation across all five rings, with intensity decreasing from R1 to R5 as expected for cascaded drop-port coupling. Mapping the drop-port spectrum onto the dimensionless control variable I via the fitted Lorentzian parameters yields 11 data points within the AEF operating range [Fig. 6(e, f)]. Over the upper operating range ($I \geq 5.8$), the integrated relative-area error between the FDTD data and the $N = 5$ theoretical curve is $\sim 11\%$, providing direct multi-ring validation of the cascade framework. The simulation was run for 120 ps, which was insufficient to reach the 10^{-5} auto-shutoff threshold (residual field energy $\sim 10^{-3}$ at termination); extending the run time would reduce spectral ringing artifacts and improve the accuracy of the extracted transfer function.

D. X-cut electrode design and EO parameters

We employ lateral signal-ground (S-G) arc electrodes on the slab surface alongside the ring waveguide (Fig. 7).

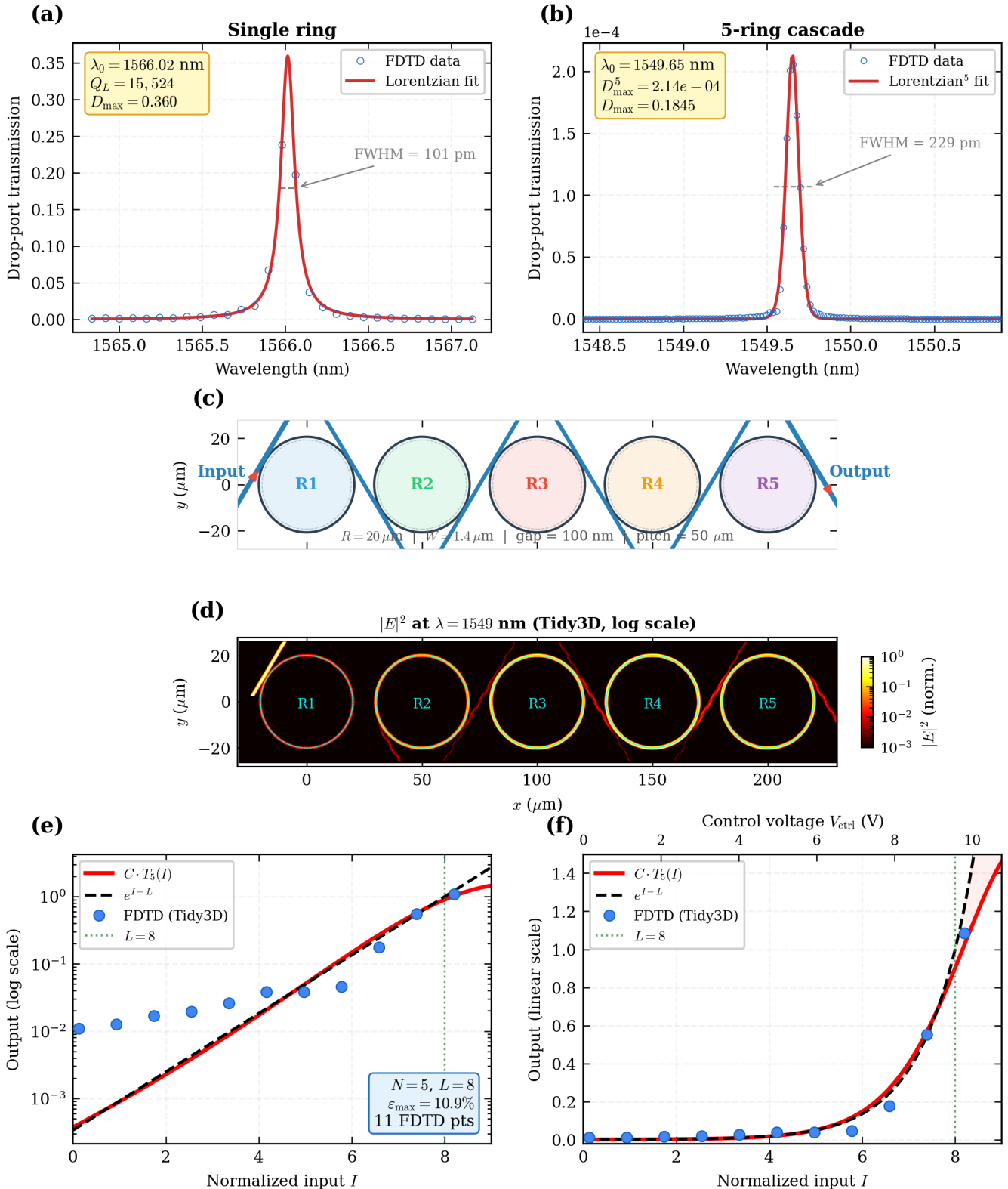


FIG. 6: FDTD-based AEF validation. (a) Lorentzian fit to the drop-port resonance at $\lambda = 1566$ nm from 3D FDTD (Lumerical) ($Q_L = 15,500$, $D_{\max} = 0.360$, $b_V = 0.182 \text{ V}^{-1}$). (b) Five-ring cascade drop-port spectrum near $\lambda_0 \approx 1550$ nm with Lorentzian⁵ fit (red curve), confirming the expected T^5 line shape. (c) Five-ring cascade MRR layout ($R = 20 \mu\text{m}$, gap = 100 nm, pitch = 50 μm) with diagonal zigzag bus waveguides. (d) $|E|^2$ field profile at $\lambda = 1549$ nm from a five-ring cascade 3D FDTD simulation (Tidy3D [43]); all five rings are resonantly excited with intensity decreasing progressively from R1 to R5. (e, f) AEF validation of the five-ring cascade: the theoretical $N = 5$ curve $C \cdot T_5(I)$ (red) and the exponential target e^{I-L} (black dashed) are compared with 11 spectral data points extracted from the Tidy3D simulation (blue circles) on log (e) and linear (f) scales. Over the upper operating range ($I \geq 5.8$), the integrated relative-area error is $\sim 11\%$; at low I ($I < 5$), the points lie above the ideal curve due to higher-order mode contamination from the oblique bus geometry.

In the X-cut orientation, the crystal Z-axis is at 45° from the horizontal in the substrate plane, giving a lateral-field projection proportional to $\cos(\theta - 45^\circ)$ at azimuthal angle θ . The $\cos(\theta - 45^\circ) = 0$ boundaries at $\theta = 135^\circ$ and 315° naturally separate the coupling regions from the electrode regions. Each ring carries a full semicircular arc electrode on the side opposite to its coupling points, engaging the large $r_{33} = 30.9 \text{ pm V}^{-1}$ Pockels coefficient [37, 38]. The effective EO fill factor follows from integrating $|\cos(\theta - 45^\circ)|$ over the semicircle:

$$f_{\text{EO}} = \frac{1}{\pi} \approx 0.318 \quad (29)$$

(see Supplementary Sec. S4 for derivation). The electrode gap is $g_{\text{el}} = 5 \text{ }\mu\text{m}$ ($d_{\text{eff}} \approx 2.5 \text{ }\mu\text{m}$), and the electro-optic overlap integral is $\Gamma_{\text{EO}} = 0.7$. Table III lists the electrode parameters.

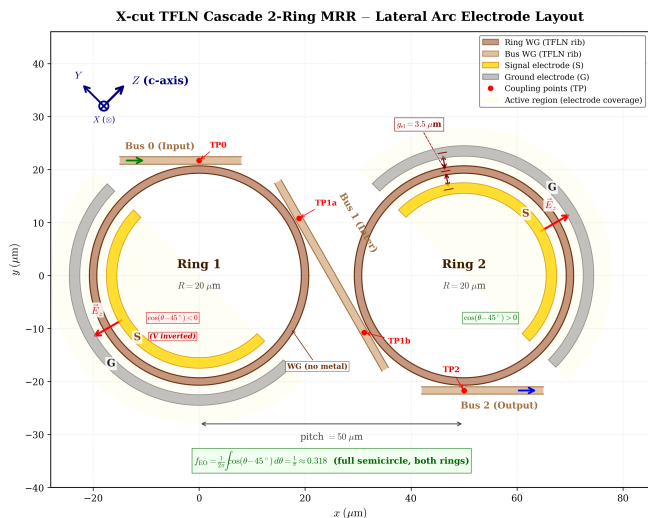


FIG. 7: Illustrative two-ring cascade layout showing the lateral S-G arc electrode placement on X-cut TFLN (the cascade design extends to N rings; this two-ring example clarifies the electrode geometry). The crystal Z-axis is oriented at 45° from the horizontal in the substrate plane. The $\cos(\theta - 45^\circ) = 0$ boundaries at $\theta = 135^\circ$ and 315° naturally separate the bus-waveguide coupling regions from the electrode semicircles: each ring carries a full semicircular arc electrode on the side opposite to its coupling points. The resulting effective EO fill factor is $f_{\text{EO}} = 1/\pi \approx 0.318$.

E. FDTD-Calibrated b_V and Cascade Optimization

From the device parameters in Tables II and III and the FDTD-calibrated $n_g \approx 2.30$, the effective normalized voltage sensitivity is (Supplementary Sec. S4; here $d\lambda/dV = 28.5 \text{ pm/V}$ is the straight-section value and f_{EO} accounts for partial electrode coverage of the ring

TABLE III: Electro-optic electrode parameters for the X-cut TFLN micro-ring with lateral S-G arc electrodes.

Parameter	Symbol	Value	Unit
Crystal orientation	—	X-cut	—
EO coefficient	r_{33}	30.9	pm V^{-1}
EO fill factor	f_{EO}	$1/\pi \approx 0.318$	—
EO overlap factor	Γ_{EO}	0.7	—
Electrode gap	g_{el}	5	μm
Effective electrode distance	d_{eff}	2.5	μm

circumference):

$$b_V = \frac{2Q(d\lambda/dV)}{\lambda_0} f_{\text{EO}} \approx 0.182 \text{ V}^{-1} \quad (30)$$

at $Q_L = 15,500$. This estimate relies on a first-order electrostatic model ($d_{\text{eff}} \approx 2.5 \text{ }\mu\text{m}$, $\Gamma_{\text{EO}} = 0.7$); a $\pm 30\%$ variation in b_V would shift the cascade depth by one to two rings at constant ε_{max} (Table IV), leaving the qualitative design conclusions unchanged. With the cascade framework of Sec. II (Eqs. 14–18), the N -ring drop-port transmission $\tilde{y}(I) = C[1 + (a + bI)^2]^{-N}$ approximates e^{I-L} over $I \in [0, L]$, with (a, b) optimized by minimax fitting for each N .

Table IV presents the optimization results for the standard dynamic range $L = 8$ ($e^8 \approx 2981$, 34.7 dB).

TABLE IV: Cascade optimization results for $L = 8$. The bias voltage $V_{\text{bias}} = |a|/b_V$ sets the DC offset, and $V_{\text{ctrl}} = bL/b_V$ is the maximum control voltage at $I = L$. Voltages computed with $b_V = 0.182 \text{ V}^{-1}$ (X-cut arc electrode, FDTD-calibrated best resonance $Q_L = 15,500$, $n_g = 2.30$). The mean FDTD quality factor across five resonances is $Q_L = 12,500 \pm 1,800$; using the mean would increase voltages by $\sim 24\%$.

N	a	b	E_∞	ε_{max} (%)	V_{bias} (V)	V_{ctrl} (V)
5	-2.0789	0.21658	0.1035	10.91	11.4	9.5
10	-1.4588	0.10202	0.0265	2.68	8.0	4.5
12	-1.3731	0.08450	0.0184	1.86	7.5	3.7
20	-1.2136	0.05025	0.0067	0.67	6.7	2.2
25	-1.1685	0.04013	0.0043	0.43	6.4	1.8
30	-1.141	0.03340	0.0030	0.30	6.3	1.5
32	-1.1301	0.03131	0.0026	0.26	6.2	1.4

^a The complete cascade optimization results for all N values are listed in Supplementary Table S7.

The approximation quality across different cascade depths is shown in Fig. 2 (Sec. III). Key thresholds (e.g., $\varepsilon < 2\%$ at $N \geq 12$, $\varepsilon < 1\%$ at $N \geq 17$) and the complete optimization results are listed in Supplementary Sec. S4.

V. PHYSICAL FEASIBILITY

Having established the cascade approximation theory (Sec. II) and the FDTD-calibrated device parameters

TABLE V: Two-regime power budget for the MRR cascade. P_{out} assumes per-channel input $P_{\text{in, ch}} = 100 \mu\text{W}$ (from a shared $P_{\text{in, tot}} = 1 \text{ mW}$ CW laser split across $M = 10$ parallel channels) and accounts only for the ideal on-resonance cascade transmission D_{max}^N (upper bound); additional inter-ring coupling loss ($\eta_{\text{coupling}} \approx 0.9$ per stage, $\sim 0.46 \text{ dB/stage}$) and off-resonance propagation loss ($0.08\text{--}0.25 \text{ dB/stage}$) are analyzed separately in Sec. V C.

	D_{max}	N	D_{max}^N	(dB)	P_{out}	ϵ_{max}
I (FDTD)	0.36	3	0.0467	-13.3	$4.67 \mu\text{W}$	$\sim 15\%$
	0.36	5	0.00605	-22.2	$0.61 \mu\text{W}$	10.9%
	0.36	7	7.84×10^{-4}	-31.1	78 nW	$\sim 5\%$
II (high- Q)	0.95	10	0.599	-2.2	$59.9 \mu\text{W}$	2.68%
	0.95	20	0.358	-4.5	$35.8 \mu\text{W}$	0.67%
	0.95	30	0.215	-6.7	$21.5 \mu\text{W}$	$\sim 0.30\%$

Regime I: FDTD-characterized ($Q_i = 38,800$). Regime II: fabricated high- Q ($Q_i > 10^6$). P_{out} scales linearly with $P_{\text{in, ch}}$.

(Sec. IV), we now assess the physical feasibility of the proposed architecture in terms of voltage requirements, insertion loss, and energy efficiency.

A. Electro-optic voltage requirements

For the primary target of $\epsilon < 2\%$ ($N = 12$), minimax optimization gives $a = -1.373$, $b = 0.0845$. With the FDTD-calibrated $Q_L = 15,500$ ($b_V = 0.182 \text{ V}^{-1}$), the required voltages are

$$V_{\text{bias}} = \frac{|a|}{b_V} = \frac{1.373}{0.182} = 7.5 \text{ V}, \quad (31)$$

$$V_{\text{ctrl, max}} = \frac{bL}{b_V} = \frac{0.0845 \times 8}{0.182} = 3.7 \text{ V}. \quad (32)$$

Since $b_V \propto Q$, voltage scales inversely with quality factor:

$$V_{\text{ctrl}} = \frac{bL}{b_V} = \frac{bL \lambda_0}{2Q |d\lambda_0/dV|}. \quad (33)$$

CMOS-compatible control voltages ($V_{\text{ctrl}} < 3.3 \text{ V}$) are achievable at $N \geq 14$ with $Q_L = 15,500$; at the design point $N = 30$ ($\epsilon_{\text{max}} = 0.30\%$), $V_{\text{ctrl}} = 1.47 \text{ V}$.

B. Power budget: two-regime analysis

The on-resonance cascade transmission D_{max}^N is the dominant contribution to total insertion loss. Table V presents two regimes: the FDTD-characterized regime ($D_{\text{max}} = 0.36$) and the fabricated high- Q regime ($D_{\text{max}} = 0.95$, achievable with $Q_i > 10^6$ and gap-optimized coupling).

In the FDTD-characterized regime, $D_{\text{max}} = 0.36$ limits practical cascades to $N \leq 5$: at $N = 5$ the output is

$0.61 \mu\text{W}$ (-22.2 dB) with $\epsilon = 10.9\%$, suited for proof-of-concept validation. In the fabricated high- Q regime ($D_{\text{max}} \geq 0.95$), deep cascades become practical: $N = 30$ yields $P_{\text{out}} = 21.5 \mu\text{W}$ (-6.7 dB) with $\epsilon_{\text{max}} \approx 0.30\%$. The transition to fabricated high- Q devices is therefore critical for achieving both high accuracy and sufficient output power.

C. Feasibility outlook

Published TFLN micro-ring resonators achieve $Q_i \geq 10^6\text{--}10^8$ using optimized fabrication [39–42]. At $Q_i = 10^6$ with the present coupling geometry, CMT predicts $D_{\text{max}} \approx 0.95$ and $Q_L \approx 25,200$ (Supplementary Sec. S5, Tables S4–S7), enabling deep cascades ($N \leq 30$) with sub-percent error. The literature values provide strong independent evidence that intrinsic quality factors in the projected range are physically achievable in TFLN—albeit with wider waveguides and larger ring radii than the present design. Transferring comparable sidewall quality to our geometry ($R = 20 \mu\text{m}$, $W = 1.4 \mu\text{m}$) is an open fabrication challenge; the projections should be read as design targets contingent on achieving it.

The total insertion loss comprises on-resonance cascade transmission D_{max}^N , inter-ring coupling loss ($\sim 0.46 \text{ dB/stage}$ for the present diagonal-bus layout), off-resonance propagation loss ($0.08\text{--}0.25 \text{ dB/stage}$), and fiber-to-chip coupling ($1.5\text{--}3.0 \text{ dB}$). For the fabricated high- Q regime ($N = 30$), the total ranges from $\sim 13 \text{ dB}$ (optimized layout) to $\sim 24 \text{ dB}$ (current geometry); see Supplementary Sec. S6 for detailed scenarios.

D. Energy comparison

For $N = 30$ X-cut TFLN micro-ring resonators in the fabricated high- Q regime ($Q_L \approx 25,200$ at $Q_i = 10^6$; Supplementary Sec. S5), the three energy components are EO tuning ($E_{\text{EO}} = 0.22 \text{ pJ}$), amortized laser ($E_{\text{laser}} = 0.07 \text{ pJ}$, shared across $M = 10$ channels), and photodetector ($E_{\text{PD}} = 0.50 \text{ pJ}$), yielding $E_{\text{photonic}} = 0.79 \text{ pJ}$ (derivations in Supplementary Sec. S7). Including thermal stabilization for $N = 30$ rings ($0.15\text{--}0.60 \text{ pJ}$; Supplementary Sec. S7), the total rises to $0.94\text{--}1.39 \text{ pJ}$.

Table S12 compares the photonic cascade with digital implementations. Including thermal stabilization ($0.94\text{--}1.39 \text{ pJ}$), the advantage over INT8 (2.3 pJ) is $1.7\text{--}2.4\times$, while operating at 10 GHz bandwidth and $58\times$ lower than digital FP32 (46 pJ). At fabricated $Q \geq 30,000$, E_{EO} drops to 0.16 pJ and $E_{\text{total}} \approx 0.73 \text{ pJ}$ (excluding thermal; Supplementary Table S11), recovering a $3.2\times$ advantage over INT8. Since $E_{\text{EO}} \propto 1/Q^2$, improving Q beyond $\sim 30,000$ yields diminishing energy returns but continues to relax CMOS driver voltage requirements.

TABLE VI: Energy per exponential operation: single-channel comparison.

Implementation	E/op (pJ)	Bandwidth	Notes
Digital FP32 (Taylor)	~ 46	1 GHz	10 FP MACs
Digital INT8 (Taylor)	~ 2.3	1 GHz	10 INT MACs
Photonic MRR ($N=30$)	0.94–1.39	10 GHz	Analog[†]

[†]0.79 pJ excluding thermal; 0.94–1.39 pJ including thermal.

Self-consistent with fabricated high- Q regime ($Q_L = 25,200$); see Supplementary Sec. S7.

VI. DISCUSSION

Practical design procedure. For a given input sequence $x = (x_1, \dots, x_K)$, the design proceeds as follows:

1. Compute $m = \max_n x_n$, $u_n = x_n - m$, and $L = -\min_n u_n$.
2. Map to nonnegative control-signal amplitudes: $I_n = u_n + L \in [0, L]$.
3. Choose tolerance ε and set $\varepsilon_{\log} = \ln(1 + \varepsilon)$.
4. Select a physically feasible b_{\max} and estimate N using Eq. (28).
5. Initialize $b = \min(b_{\max}, 1/N)$ and $a = -1 - bL/2$, then refine (a, b) by a two-parameter minimax fit if required.
6. The optical block yields $\tilde{y}(I_n) \approx e^{x_n - m}$, and softmax weights follow as

$$p_n = \frac{\tilde{y}(I_n)}{\sum_j \tilde{y}(I_j)}. \quad (34)$$

Scope and limits. The approximation is for a finite interval $I \in [0, L]$, where L is determined by the input batch via Eq. (4). In practice, one designs for a worst-case L expected in operation (or retunes a and rescales the control signal to adapt L). Noise, insertion loss, and control-induced parasitics limit accuracy and dynamic range; we treat these effects as platform-specific margins. Detailed non-ideality assumptions, parameter distributions, and robustness statistics are reported in Supplementary Sec. S8. With K channels in parallel, one can form softmax by summing channel powers and applying a shared reciprocal scale factor, depending on the chosen mixed-signal normalization scheme.

Why cascade helps. A single Lorentzian in I is too rigid to mimic the log-linear target over a wide interval. Cascading turns the transfer into a product; taking a logarithm gives a sum of smooth terms, and the approximation improves as N increases. The slope constraint $N|b| \gtrsim 1$ is an immediate feasibility check.

Global softmax normalization via probe-intensity feedback. Multiple AEF blocks can be arranged in parallel (Fig. 8), with a shared probe-intensity

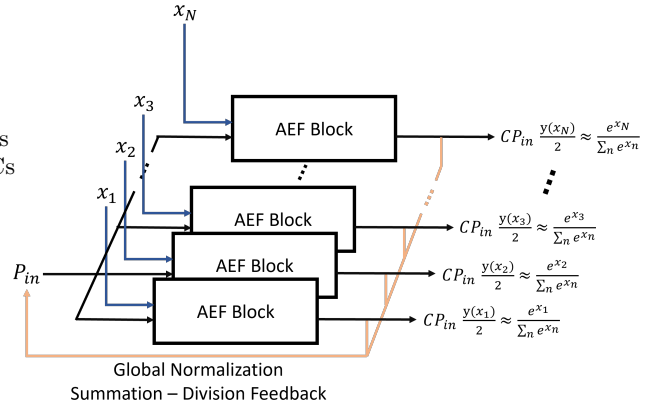


FIG. 8: Conceptual three-head parallel AEF architecture for softmax-oriented computation. Each head processes its input through an AEF (Approximate Exponential Function) block to generate channel-wise exponential responses, while a shared global feedback path aggregates head outputs and provides normalization-consistent scaling (SDF: Summation–Division Feedback). The three-head drawing is illustrative and generalizes to H parallel heads.

feedback path providing global normalization. A PI loop or feedforward reciprocal estimation can regulate the summed output to a fixed reference, yielding softmax-consistent weights [44, 45]. Design details and stability analysis are provided in Supplementary Sec. S9.

Beyond ring-resonator AEF implementations, the same cascade principle can be extended to other cavity-based photonic platforms, such as serial 1D photonic-crystal cavities and other cascaded resonant architectures [21, 46]. What these platforms share is transfer-function shaping through cascaded resonances; loss, tuning range, fabrication tolerance, and calibration overhead remain platform-dependent.

The insertion loss budget (Sec. V C) and electro-optic voltage requirements (Sec. V A) suggest that the cascade architecture is feasible under optimized coupling and layout conditions. Using monolithic TFLN microring data from Bahadori *et al.* [47] ($Q \approx 5432$, $d\lambda_0/dV \approx 9\text{--}20$ pm/V), the normalized sensitivity $b_V \simeq 0.063\text{--}0.14$ V⁻¹, within the range required by the cascade design.

Crystal orientation and electrode design. The X-cut TFLN platform was chosen for several reasons. First, X-cut is the prevailing industry standard for integrated TFLN modulators, with well-established fabrication processes and commercial wafer availability [37, 38]. Second, the TE₀ mode—which is strongly confined in the rib waveguide geometry—can engage the large r_{33} coefficient via lateral electric fields aligned with the crystal Z-axis. In contrast, Z-cut geometry with TE polarization can only access the smaller r_{13} coefficient (~ 10 pm/V), resulting in significantly lower electro-optic efficiency. The arc electrode design (Sec. IV D) addresses the phase-cancellation

problem inherent to X-cut circular rings [47] by orienting the crystal Z-axis at 45° from the horizontal in the substrate plane. This rotation places the $\cos(\theta - 45^\circ) = 0$ boundaries at $\theta = 135^\circ$ and 315° , naturally separating the bus-waveguide coupling regions from the electrode regions. Each ring carries a full semicircular arc electrode on the side opposite to its coupling points, yielding an effective fill factor $f_{\text{EO}} = 1/\pi \approx 0.318$. While this reduces the round-trip EO efficiency compared to a hypothetical full-circumference design, it preserves the compact footprint of a circular ring resonator. The cascade performance can be further improved beyond the $R = 20 \mu\text{m}$ circular-ring design presented here. Increasing the ring radius reduces bending loss and raises the intrinsic quality factor Q_i , which directly increases b_V ($\propto Q$) and lowers the required control voltage. Alternatively, adopting a race-track geometry with extended straight coupling sections strengthens the bus-ring coupling, pushing the drop-port maximum D_{max} closer to critical coupling and improving the per-stage transfer efficiency. Either approach—or their combination—would yield higher b_V and D_{max} , enabling lower N or tighter approximation accuracy at reduced operating voltages.

Fabrication considerations. The X-cut TFLN rib waveguide (600 nm total thickness, 500 nm etch, $w = 1.4 \mu\text{m}$) follows established fabrication processes for commercial TFLN wafers on SiO_2 [37, 38]. The lateral signal-ground (SG) electrode configuration is fabricated in a single metal layer, which is standard in TFLN foundry processes. The primary fabrication challenge for the cascade architecture is maintaining uniform coupling gaps ($g = 100 \text{ nm}$) across N rings to ensure identical Lorentzian transfer functions. Post-fabrication trimming via UV exposure or localized thermal oxidation can compensate residual detuning variations [30], as quantified in the Monte Carlo robustness analysis (Supplementary Sec. S8). Monte Carlo simulations (Supplementary Sec. S8) show that under nominal non-ideality levels ($\sigma_a = 0.020$, $\sigma_{b,\text{rel}} = 0.020$), a single-point calibration of C per chip keeps the median softmax KL divergence below 2.2×10^{-4} , with 95th-percentile max probability error under 0.32%. Even under stress conditions ($\sigma_a = 0.032$), 95th-percentile errors remain below 0.42%, demonstrating that the identical-detuning design is robust to realistic fabrication variations provided a per-chip calibration step is performed. Conversely, if coupling gaps are intentionally varied across rings, the per-ring parameters (a_k, b_k) become independent degrees of freedom. A Taylor-expansion analysis shows that K non-identical rings can cancel curvature terms up to order $2K$ in the Taylor series of $g(I) = \sum_k \ln T_k$, one order higher than K identical rings, so that fewer rings suffice for a given error target.

TABLE VII: Summary of evidence levels for key claims.

Claim	Evidence	Sec.
Cascade \rightarrow exp. approx.	Analytic	II
Depth scaling	Analytic + num.	II, III
Q_L, D_{max}, b_V	3-D FDTD	IV
5-ring line shape	3-D FDTD	IV
$N \leq 30$ deep cascade	CMT proj.*	V
Energy $< 1 \text{ pJ}$	Estimate	V
Full softmax	Conceptual	VI

*Based on published $Q_i \geq 10^6$ values [39, 42] and CMT coupling model.

VII. CONCLUSION

We have presented a cascaded micro-ring resonator architecture that approximates the exponential function $e^{x_n - m}$ on a finite interval $[0, L]$ using multiplicative Lorentzian transfer functions. Increasing the cascade depth N systematically reduces the worst-case relative error, and an identical-detuning design initialized by flank and slope matching provides a practical two-parameter design.

Three-dimensional FDTD simulations of a single X-cut TFLN add-drop ring ($R = 20 \mu\text{m}$, $g = 100 \text{ nm}$) yield $Q_L = 10,300$ – $15,500$ and $D_{\text{max}} \approx 0.36$, calibrating the cascade transfer model. A five-ring cascade 3D FDTD simulation directly validates the multi-ring framework: all five rings exhibit resonant excitation, and mapping the drop-port spectrum onto the dimensionless control variable reproduces the theoretical $N = 5$ curve with $\sim 11\%$ integrated relative-area error over the upper operating range ($I \geq 5.8$), providing the first multi-ring confirmation of the cascade exponential approximation. At the present FDTD-characterized quality factor, practical cascades are limited to $N = 5$ – 7 ($\varepsilon \lesssim 11\%$). If high- Q TFLN resonators reported in the literature ($Q_i \geq 10^6$, $D_{\text{max}} \geq 0.95$) are realized in the cascade geometry, deeper cascades ($N \approx 20$ – 30) would reach sub-percent approximation error with an estimated per-operation energy of 0.79 – 1.39 pJ , which is 1.7 – $2.4\times$ lower than an INT8 MAC at the 7 nm node. Monte Carlo analysis shows that the identical-detuning design tolerates realistic fabrication variations ($\sigma_a = 0.020$, $\sigma_{b,\text{rel}} = 0.020$) with a single per-chip calibration, keeping the 95th-percentile softmax probability error below 0.32%.

The formulation is not restricted to electro-optic tuning; it requires only a controllable detuning coordinate with local linearization, so both Pockels and optical (Kerr/XPM) mechanisms are compatible [37, 38, 47, 48]. We demonstrate a photonic exponential block and outline a plausible mixed-signal path toward full softmax normalization; completing a full softmax additionally requires max-finding, summation, and reciprocal circuitry, which remain open for future experimental validation.

-
- [1] Ashish Vaswani, Noam Shazeer, Niki Parmar, Jakob Uszkoreit, Llion Jones, Aidan N. Gomez, Lukasz Kaiser, and Illia Polosukhin. Attention is all you need. In *Advances in Neural Information Processing Systems 30 (NeurIPS 2017)*, pages 5998–6008, 2017.
- [2] Tri Dao, Daniel Y. Fu, Stefano Ermon, Atri Rudra, and Christopher Ré. FlashAttention: Fast and memory-efficient exact attention with IO-awareness. In *Advances in Neural Information Processing Systems 35 (NeurIPS 2022)*, pages 16344–16359, 2022.
- [3] Neil Savage. Light could lower AI’s appetite for power. *Nature Nanotechnology*, 21:6–8, 2026.
- [4] Yichen Shen et al. Deep learning with coherent nanophotonic circuits. *Nature Photonics*, 11(7):441–446, 2017.
- [5] Johannes Feldmann et al. Parallel convolutional processing using an integrated photonic tensor core. *Nature*, 589(7840):52–58, 2021.
- [6] Nicholas C. Harris et al. Linear programmable nanophotonic processors. *Optica*, 5(12):1623–1631, 2018.
- [7] Bowei Dong, Samarth Aggarwal, Wen Zhou, Utku Emre Ali, Nikolaos Farmakidis, June Sang Lee, Yuhan He, Xuan Li, Dim-Lee Kwong, C. D. Wright, Wolfram H. P. Pernice, and H. Bhaskaran. Higher-dimensional processing using a photonic tensor core with continuous-time data. *Nature Photonics*, 17(12):1080–1088, 2023.
- [8] Sudip Shekhar, Wim Bogaerts, Lukas Chrostowski, John E. Bowers, Michael Hochberg, Richard Soref, and Bhavin J. Shastri. Roadmapping the next generation of silicon photonics. *Nature Communications*, 15:751, 2024.
- [9] Mario Miscuglio and Volker J. Sorger. Photonic tensor cores for machine learning. *Applied Physics Reviews*, 7(3):031404, 2020.
- [10] Yaowen Hu, Yunxiang Song, Xinrui Zhu, Xiangwen Guo, Shengyuan Lu, Qihang Zhang, Lingyan He, C. A. A. Franken, Keith Powell, Hana Warner, Daniel Assumpcao, Dylan Renaud, Ying Wang, et al. Integrated lithium niobate photonic computing circuit based on efficient and high-speed electro-optic conversion. *Nature Communications*, 16:8178, 2025.
- [11] Priyabrata Dash, Anxiao Jiang, and Dharanidhar Dang. SOFTONIC: A photonic design approach to softmax activation for high-speed fully analog AI acceleration. In *Proceedings of the Great Lakes Symposium on VLSI (GLSVLSI ’25)*, pages 118–125, 2025.
- [12] Ziyu Zhan, Hao Wang, Qiang Liu, and Xing Fu. Optoelectronic nonlinear softmax operator based on diffractive neural networks. *Optics Express*, 32(15):26458–26469, 2024.
- [13] Ye Tian, Shuiying Xiang, Xingxing Guo, Yahui Zhang, Jiashang Xu, Shangxuan Shi, Haowen Zhao, Yizhi Wang, Xinran Niu, Wenzhuo Liu, and Yue Hao. Photonic transformer chip: interference is all you need. *Photonix*, 6:45, 2025.
- [14] Jacob R. Stevens, Rangharajan Venkatesan, Steve Dai, Bruce Khailany, and Anand Raghunathan. Softmax: Hardware/software co-design of an efficient softmax for transformers. In *Proceedings of the 58th ACM/IEEE Design Automation Conference (DAC)*, pages 469–474, 2021.
- [15] Nazim Altar Koca, Anh Tuan Do, and Chip-Hong Chang. Hardware-efficient softmax approximation for self-attention networks. In *Proceedings of the IEEE International Symposium on Circuits and Systems (ISCAS)*, pages 1–5, 2023.
- [16] Wenxun Wang, Shuchang Zhou, Wenyu Sun, Peiqin Sun, and Yongpan Liu. SOLE: Hardware-software co-design of softmax and layernorm for efficient transformer inference. In *Proceedings of the IEEE/ACM International Conference on Computer-Aided Design (ICCAD)*, pages 1–9, 2023.
- [17] Yuan Zhang, Yonggang Zhang, Lele Peng, Lianghua Quan, Shubin Zheng, Zhonghai Lu, and Hui Chen. Base-2 softmax function: Suitability for training and efficient hardware implementation. *IEEE Transactions on Circuits and Systems I: Regular Papers*, 69(9):3605–3618, 2022.
- [18] Zhengyu Mei, Hongxi Dong, Yuxuan Wang, and Hongbing Pan. TEA-S: A tiny and efficient architecture for PLAC-based softmax in transformers. *IEEE Transactions on Circuits and Systems II: Express Briefs*, 70:3594–3598, 2023.
- [19] Ke Chen, Yue Gao, Haroon Waris, Weiqiang Liu, and Fabrizio Lombardi. Approximate softmax functions for energy-efficient deep neural networks. *IEEE Transactions on Very Large Scale Integration (VLSI) Systems*, 31:4–16, 2023.
- [20] Wim Bogaerts et al. Silicon microring resonators. *Laser & Photonics Reviews*, 6(1):47–73, 2012.
- [21] John E. Heebner, Robert W. Boyd, and Q.-Han Park. Scissor solitons and other propagation effects in microresonator-modified waveguides. *Journal of the Optical Society of America B*, 19(4):722–731, 2002.
- [22] Jiahui Wang, Sean P. Rodrigues, Ercan M. Dede, and Shanhui Fan. Microring-based programmable coherent optical neural networks. *Optics Express*, 31(12):18871, 2023.
- [23] Pengxing Guo, Niujie Zhou, Weigang Hou, and Lei Guo. StarLight: a photonic neural network accelerator featuring a hybrid mode-wavelength division multiplexing and photonic nonvolatile memory. *Optics Express*, 30:37051, 2022.
- [24] Weizhen Yu, Shuang Zheng, Zhenyu Zhao, Bin Wang, and Weifeng Zhang. Reconfigurable low-threshold all-optical nonlinear activation functions based on an add-drop silicon microring resonator. *IEEE Photonics Journal*, 14(6):1–7, 2022.
- [25] Bahaa E. A. Saleh and Malvin C. Teich. *Fundamentals of Photonics*. Wiley, Hoboken, NJ, 2 edition, 2007.
- [26] Vítor R. Almeida, Carlos A. Barrios, Roberto R. Panepucci, and Michal Lipson. All-optical control of light on a silicon chip. *Nature*, 431(7012):1081–1084, 2004.
- [27] Qianfan Xu, Bradley Schmidt, Sameer Pradhan, and Michal Lipson. Micrometre-scale silicon electro-optic modulator. *Nature*, 435(7040):325–327, 2005.
- [28] Kishore Padmaraju and Keren Bergman. Resolving the thermal challenges for silicon microring resonator devices. *Nanophotonics*, 3:269–281, 2014.
- [29] Erwen Li, Behzad Ashrafi Nia, Bokun Zhou, and Alan X. Wang. Transparent conductive oxide-gated silicon microring with extreme resonance wavelength tunability. *Photonics Research*, 7(4):473, 2019.
- [30] Lahiru Jayatileka et al. Post-fabrication trimming of silicon photonic ring resonators at wafer-scale. *Journal*

- of *Lightwave Technology*, 39:5083–5088, 2021.
- [31] Elliott W. Cheney. *Introduction to Approximation Theory*. McGraw–Hill, New York, 1966.
- [32] Alec Radford et al. Language models are unsupervised multitask learners. Technical report, OpenAI, 2019.
- [33] Hugging Face. distilgpt2 model card, 2025. accessed 2026-02-21.
- [34] Andrej Karpathy. Tiny shakespeare dataset (char-rnn), 2025. accessed 2026-02-21.
- [35] Jane Austen. Pride and prejudice. Project Gutenberg eBook No. 1342, 2025. accessed 2026-02-21.
- [36] Hyoseok Park. MRR-AEF: reproducible MRR depth-sweep fitting and supplementary validation scripts. GitHub repository, 2025. commit 585e695, accessed 2026-02-21.
- [37] Di Zhu et al. Integrated photonics on thin-film lithium niobate. *Advances in Optics and Photonics*, 13(2):242–352, 2021.
- [38] Yaowen Hu, Di Zhu, Shengyuan Lu, Xinrui Zhu, Yunxiang Song, Dylan Renaud, Daniel Assumpcao, Rebecca Cheng, CJ Xin, Matthew Yeh, Hana Warner, Xiangwen Guo, Amirhassan Shams-Ansari, David Barton, Neil Sinclair, and Marko Loncar. Integrated electro-optics on thin-film lithium niobate. *Nature Reviews Physics*, 2025.
- [39] Mian Zhang, Cheng Wang, Rebecca Cheng, Amirhassan Shams-Ansari, and Marko Loncar. Monolithic ultra-high-Q lithium niobate microring resonator. *Optica*, 4(12):1536–1537, 2017.
- [40] Rongjin Zhuang, Jinze He, Yifan Qi, and Yang Li. High-Q thin-film lithium niobate microrings fabricated with wet etching. *Adv. Mater.*, 35(3):2208113, 2023.
- [41] Xinrui Zhu, Yaowen Hu, Shengyuan Lu, Hana K. Warner, Xudong Li, Yunxiang Song, Letícia S. Magalhães, Amirhassan Shams-Ansari, Neil Sinclair, and Marko Loncar. Twenty-nine million intrinsic Q-factor monolithic microresonators on thin-film lithium niobate. *Photon. Res.*, 12(8):A63–A68, 2024.
- [42] Renhong Gao, Ni Yao, Jianglin Guan, Li Deng, Jintian Lin, Min Wang, Lingling Qiao, Wei Fang, and Ya Cheng. Lithium niobate microring with ultra-high Q factor above 10^8 . *Chin. Opt. Lett.*, 20(1):011902, 2022.
- [43] Flexcompute Inc. Tidy3D: electromagnetic simulation software. <https://www.flexcompute.com/tidy3d/>, 2024. v2.10; cloud GPU FDTD. See also the accompanying Tidy3D example notebook.
- [44] John K. Doylend, Paul E. Jessop, and Andrew P. Knights. Silicon photonic dynamic optical channel leveler with external feedback loop. *Optics Express*, 18(13):13805–13812, 2010.
- [45] Karl J. Åström and Richard M. Murray. *Feedback Systems: An Introduction for Scientists and Engineers*. Princeton University Press, Princeton, NJ, 2008.
- [46] Amnon Yariv, Yong Xu, Reginald K. Lee, and Axel Scherer. Coupled-resonator optical waveguide: a proposal and analysis. *Optics Letters*, 24(11):711–713, 1999.
- [47] Meisam Bahadori, Yansong Yang, Ahmed E. Hassanien, Lynford L. Goddard, and Songbin Gong. Ultra-efficient and fully isotropic monolithic microring modulators in a thin-film lithium niobate photonics platform. *Optics Express*, 28(20):29644–29661, 2020.
- [48] Abu Naim R. Ahmed, Shouyuan Shi, Mathew Zablocki, Peng Yao, and Dennis W. Prather. Tunable hybrid silicon nitride and thin-film lithium niobate electro-optic microresonator. *Optics Letters*, 44(3):618, 2019.

SUPPLEMENTARY INFORMATION

Supplementary material accompanying “Photonic Exponential Approximation via Cascaded TFLN Microring Resonators toward Softmax.”

S0. RIGOROUS DERIVATION AND VALIDITY SCOPE

This section derives the depth-scaling relations and screening bounds used in the main text, and states the assumptions under which they apply, together with validity scope and failure cases. We separate proved statements (Lemma, Proposition, Theorem) from heuristic engineering estimates that rely on empirical calibration.

S0.1 Assumptions

Assumption 1 (Lorentzian single-ring transfer). *Each ring k has a normalized add-to-drop transmission of the form $T_k(I) = [1 + (a_k + bI)^2]^{-1}$, where $a_k \in \mathbb{R}$ is the dimensionless static detuning, $b > 0$ is the common normalized sensitivity, and $I \geq 0$ is a nonnegative control-signal amplitude.*

Assumption 2 (Multiplicative cascade). *The N rings are cascaded in a serial add-drop topology (the drop output of ring k feeds the add input of ring $k+1$), and the probe is sufficiently weak that cross-ring and nonlinear probe-induced effects are negligible; thus the total normalized transmission is $y(I) = \prod_{k=1}^N T_k(I)$.*

Assumption 3 (Identical-detuning family). *All rings share the same static detuning: $a_1 = \dots = a_N \equiv a$. This reduces the design space to (a, b) and a global scale $C > 0$; the scaled output is $\tilde{y}(I) = C [1 + (a + bI)^2]^{-N}$.*

Assumption 4 (Linear control-to-resonance mapping). *Within the operating range $I \in [0, L]$, the resonance shift is a linear function of the control-signal amplitude (Eq. (10) of main text), i.e., higher-order detuning nonlinearity is negligible.*

Assumption 5 (Finite interval and bounded L). *The approximation target is $f(I) = e^{I-L}$ on a finite interval $I \in [0, L]$ with $L > 0$ determined by the input batch ($L = \max(x) - \min(x)$). The depth-scaling results are derived for fixed, finite L .*

Assumption 6 (Flank-centered operating regime). *The design uses the “flank-centered” initialization: $a + b(L/2) = -1$ (midpoint on the Lorentzian half-maximum) and $Nb = 1$ (slope matching). This places the operating point in the steepest-slope region of the Lorentzian, where the log-transfer is most nearly linear.*

S0.2 Rigorous results

Throughout, define the log-domain residual

$$r(I) \equiv \ln \tilde{y}(I) - (I - L) = \ln C - N \ln(1 + (a + bI)^2) - (I - L), \quad (\text{S0.1})$$

and the worst-case log-error $E_\infty = \sup_{I \in [0, L]} |r(I)|$. We set C to the minimax-optimal value $\ln C^* = -(\max_I g(I) + \min_I g(I))/2$, where $g(I) = \ln y(I) - (I - L)$, throughout.

Lemma 1 (Slope bound — rigorous). *Under Assumptions 1–3, for every $I \geq 0$,*

$$\left| \frac{d}{dI} \ln y(I) \right| \leq N |b|.$$

Proof. From Assumption 3, $\ln y(I) = -N \ln(1 + (a + bI)^2)$. Differentiating:

$$\frac{d}{dI} \ln y(I) = -N \frac{2b(a + bI)}{1 + (a + bI)^2}.$$

Let $u \equiv a + bI \in \mathbb{R}$. The function $h(u) = 2u/(1 + u^2)$ satisfies $|h(u)| \leq 1$ for all $u \in \mathbb{R}$ (since $1 + u^2 \geq 2|u|$ by AM–GM). Therefore $|d(\ln y)/dI| = N|b| |h(u)| \leq N|b|$. \square

Remark 1 (Necessary condition for approximation). *Since the target $\ln f(I) = I - L$ has constant slope +1, a necessary condition for the cascade log-transfer to track this slope at any point is $N|b| \geq 1$. This is Eq. (23) of the main text and is a rigorous (not heuristic) necessary condition.*

Proposition 1 (Log-domain Taylor expansion at flank center). *Under Assumptions 1–6, define $I_0 = L/2$ and $\delta = I - I_0$. Then*

$$\ln \tilde{y}(I) = \text{const} + \delta + \frac{\delta^3}{6N^2} + R_4(\delta), \quad (\text{S0.2})$$

where $|R_4(\delta)| \leq M_4 \delta^4$ with $M_4 = N|b|^4 \cdot \sup_{|\delta| \leq L/2} |q^{(4)}(u(\delta))|$ and $q(u) = -\ln(1+u^2)$. In particular, the quadratic term vanishes identically at the flank point $u_0 = a + bI_0 = -1$.

Proof. Set $u(\delta) = a + b(I_0 + \delta) = -1 + b\delta$ (using $a + bI_0 = -1$). Define $\phi(u) = -\ln(1+u^2)$. Then $\ln y(I) = N\phi(u(\delta))$ and $u'(\delta) = b$. Compute derivatives of ϕ at $u_0 = -1$:

$$\begin{aligned} \phi'(u) &= -\frac{2u}{1+u^2}, & \phi'(-1) &= 1, \\ \phi''(u) &= \frac{2(u^2-1)}{(1+u^2)^2}, & \phi''(-1) &= 0, \\ \phi'''(u) &= \frac{4u(3-u^2)}{(1+u^2)^3}, & \phi'''(-1) &= \frac{-4(-1)(3-1)}{(1+1)^3} = 1. \end{aligned}$$

By the chain rule, writing $F(\delta) = N\phi(u(\delta))$:

$$\begin{aligned} F'(0) &= Nb\phi'(-1) = Nb = 1, \\ F''(0) &= Nb^2\phi''(-1) = 0, \\ F'''(0) &= Nb^3\phi'''(-1) = Nb^3 = \frac{1}{N^2}, \end{aligned}$$

where we used $b = 1/N$ from Assumption 6 in the last step. Hence the Taylor expansion with the minimax-optimal C is

$$\ln \tilde{y}(I) = \text{const} + \delta + 0 \cdot \frac{\delta^2}{2} + \frac{1}{N^2} \cdot \frac{\delta^3}{6} + R_4(\delta).$$

Subtracting the target δ (the linear part of $I - L$ around I_0) gives a leading residual $\delta^3/(6N^2)$. The remainder is bounded by the standard Taylor remainder estimate. \square

Theorem 1 (Heuristic depth-scaling law). *Under Assumptions 1–6 and ignoring the fourth-order remainder R_4 , the leading-order worst-case log-error on $I \in [0, L]$ satisfies*

$$E_\infty^{(\text{leading})} \sim \frac{1}{6N^2} \left(\frac{L}{2}\right)^3 = \frac{L^3}{48N^2}. \quad (\text{S0.3})$$

Setting $E_\infty^{(\text{leading})} \leq \varepsilon_{\log} = \ln(1+\varepsilon)$ and solving for N gives

$$N \geq \frac{L^{3/2}}{\sqrt{48\varepsilon_{\log}}}. \quad (\text{S0.4})$$

Derivation (heuristic). From Proposition 1, the residual with respect to the target is dominated by $\delta^3/(6N^2)$ for $|\delta| \leq L/2$. The maximum of $|\delta|^3$ on $[-L/2, L/2]$ is $(L/2)^3$. Setting the bound equal to ε_{\log} and solving:

$$\frac{L^3}{48N^2} \leq \varepsilon_{\log} \implies N \geq \frac{L^{3/2}}{\sqrt{48\varepsilon_{\log}}}.$$

With $1/\sqrt{48} \approx 0.144$, and accounting for the fact that the minimax-optimal residual is typically smaller than the one-sided Taylor bound by a factor of ~ 2 (equi-oscillation), the effective prefactor becomes $\kappa \approx 0.07$, yielding the main-text engineering estimate Eq. (28): $N \approx \lceil \max(1/b_{\max}, \kappa L^{3/2}/\sqrt{\varepsilon_{\log}}) \rceil$. \square

Remark 2 (Status of Theorem 1). *This is a heuristic scaling law, not a rigorous minimax guarantee. The derivation truncates the Taylor series at third order and approximates the equi-oscillation factor empirically ($\kappa \approx 0.07$). For a rigorous bound one would need explicit control of R_4 over the full interval $[0, L]$, which depends on L, N , and higher derivatives of the Lorentzian; we do not claim such a bound here. The scaling $N \sim L^{3/2}/\sqrt{\varepsilon_{\log}}$ is supported by numerical evidence (Table I) but should be treated as an engineering design rule.*

S0.3 Derivation of the conservative screening bound

We now derive the conservative screening bound (Eqs. S0.7–S0.8 below), which is stated inline in Sec. II of the main text.

Proposition 2 (Conservative log-error bound). *Under Assumptions 1–5 (identical detuning, but not restricted to the flank-centered choice), fix $b > 0$ and choose the normalization $\tilde{y}(L) = 1$. Define $\phi(u) = -\ln(1 + u^2)$ and write*

$$\ln \tilde{y}(I) = N[\phi(a + bI) - \phi(a + bL)].$$

The target in this normalization is $(I - L)$. Denoting the residual $r(I) = \ln \tilde{y}(I) - (I - L)$, we have $r(L) = 0$ and $r(0) = N[\phi(a) - \phi(a + bL)] + L$.

For any choice of a such that the operating range $\{a + bI : I \in [0, L]\}$ lies in the region where ϕ is concave (i.e., $\phi''(u) \leq 0$ throughout), the worst-case log-error satisfies

$$E_\infty \leq \frac{N\|\phi''\|_\infty b^2 L^2}{8} + \left| \frac{N\phi'(a + bL) \cdot b - 1}{2} \right| \cdot L, \quad (\text{S0.5})$$

where $\|\phi''\|_\infty = \sup_{u \in [a, a+bL]} |\phi''(u)|$.

Derivation sketch. Write $h(I) \equiv N\phi(a + bI)$. The slope is $h'(I) = Nb\phi'(a + bI)$. At $I = L$, we want the slope to match the target slope 1; define the slope mismatch $\Delta s \equiv h'(L) - 1 = Nb\phi'(a + bL) - 1$. By the mean-value theorem on $[0, L]$:

$$r(I) - r(L) = r(I) = [h(I) - h(L)] - (I - L) = \int_I^L [1 - h'(t)] dt.$$

Write $1 - h'(t) = (1 - h'(L)) + (h'(L) - h'(t)) = -\Delta s + \int_t^L h''(s) ds$. Since $h''(s) = Nb^2\phi''(a + bs)$, we bound $|h''(s)| \leq Nb^2\|\phi''\|_\infty$. Integrating twice and applying the triangle inequality gives (S0.5). \square

Corollary 1 (Main-text conservative bound). *Under slope matching at $I = L$ (i.e., $Nb\phi'(a + bL) = 1$, so $\Delta s = 0$), and using $\|\phi''\|_\infty \leq 2$ (which holds since $|\phi''(u)| = |2(u^2 - 1)/(1 + u^2)^2| \leq 2$ for all $u \in \mathbb{R}$), the bound simplifies to*

$$E_\infty \leq \frac{Nb^2 L^2}{4}. \quad (\text{S0.6})$$

Using $b = 1/N$ (the slope-matching choice from $Nb = 1$) gives $E_\infty \leq L^2/(4N)$. If instead we retain a general b but add the penalty from imperfect slope matching (e.g., from the constraint $b \leq b_{\max}$), a combined conservative bound is

$$E_\infty \leq \frac{L^2}{4N} + \frac{1}{2b^2 N}, \quad (\text{S0.7})$$

which provides a conservative heuristic bound on the log-error. Setting this $\leq \ln(1 + \varepsilon)$ and solving for N yields the conservative screening depth:

$$N_{\text{safe}} \geq \left\lceil \frac{L^2/4 + 1/(2b^2)}{\ln(1 + \varepsilon)} \right\rceil. \quad (\text{S0.8})$$

Remark 3 (Status of the conservative bound). *Equation (S0.7) is a **conservative heuristic design rule**. It is conservative because: (i) we use a global upper bound $\|\phi''\|_\infty \leq 2$ instead of the actual curvature, (ii) we do not exploit the minimax-optimal C shift. It is heuristic (not a formal guarantee) because: (i) the derivation assumes the operating range lies in the concavity region of ϕ , which may not hold for all detuning choices; (ii) the second term $1/(2b^2 N)$ arises from a simplified penalty model for flank-curvature mismatch that has not been proved to be a rigorous upper bound in all parameter regimes. N_{safe} from Eq. (S0.8) is therefore a **screening estimate**, suitable for preliminary design-space exploration but not a certified minimax guarantee.*

S0.4 Validity scope and failure cases

The derivations above hold under the stated assumptions. We now identify the regimes where each assumption may break down.

- (V1) **Lorentzian model (A1)**. The single-ring Lorentzian form $T = [1 + (a + bI)^2]^{-1}$ is a near-resonance approximation valid when the probe frequency is within a few linewidths of the resonance. Far from resonance, higher-order dispersion, Fano interference, or multi-mode effects introduce deviations. *Failure case*: operation with very large detuning ($|a + bI| \gg 1$ across the full interval), where the Lorentzian tails may not be accurate for high- Q rings.
- (V2) **Multiplicative cascade (A2)**. Requires that inter-ring reflections and back-scattering are negligible (forward-propagating coupling only, i.e. negligible back-reflection at each inter-ring junction). *Failure case*: very high ring count N with non-negligible back-reflection per stage, which can produce Fabry–Pérot-like ripples in the cascade transfer function.
- (V3) **Identical-detuning family (A3)**. The Taylor expansion and conservative bound both assume $a_1 = \dots = a_N$. In practice, fabrication variations introduce per-ring detuning spread σ_a . The Monte Carlo analysis in Sec. S8 quantifies robustness, but the *analytical* bounds (S0.2)–(S0.8) are strictly valid only for identical detuning.
- (V4) **Linear control-to-resonance mapping (A4)**. The linearized model $\omega_0(I) = \omega_0^{(0)} + \eta I$ introduces systematic error at large control amplitudes. For carrier-injection (free-carrier plasma effect) or thermal tuning over wide ranges, second-order nonlinearity in the control-to-detuning mapping can exceed 1%. *Failure case*: large L requiring a control swing exceeding the linearity range of the tuning mechanism.
- (V5) **Finite interval (A5)**. All bounds scale with L (typically as L^2 or $L^{3/2}$). As $L \rightarrow \infty$, N grows without bound and insertion loss accumulates ($\sim N \cdot IL_{\text{stage}}$), eventually degrading the probe SNR below the useful regime. There is no finite N that works for all L simultaneously. *Practical regime*: $L \lesssim 10$ – 12 (consistent with L_{eff} at p90–p95 from Sec. S3) is the primary target; $L \gtrsim 16$ requires $N \gtrsim 30$ even for moderate tolerance, pushing loss budgets.
- (V6) **Flank-centered initialization (A6)**. The Taylor-based scaling (Theorem 1) relies on the cancellation $\phi''(-1) = 0$ at the half-maximum point. If the operating point deviates (e.g., due to fabrication offset pushing $a + bI_0$ away from -1), a nonzero quadratic residual appears and the effective scaling worsens to $E_\infty \sim L^2/N$ rather than L^3/N^2 . *Mitigation*: heater/bias trimming to restore the flank condition.

S0.5 Mapping to main-text equations

For reference, the results derived here correspond to the following main-text equations:

- **Slope bound** (Lemma 1): rigorous; corresponds to main-text Eqs. (22)–(23). This is a *guaranteed* necessary condition.
- **Engineering N -estimate** (Theorem 1): heuristic scaling with empirical prefactor $\kappa \approx 0.07$; corresponds to main-text Eq. (28). This is a *heuristic design rule* calibrated against numerical fits.
- **Conservative bound** (Corollary 1): conservative but not rigorously certified as a minimax upper bound; derived as Eq. (S0.7) in this supplement, stated inline in Sec. II. This is a *conservative heuristic screening condition*.
- N_{safe} (Corollary 1, Eq. S0.8): the safe screening depth derived from the conservative bound; derived as Eq. (S0.8) in this supplement, stated inline in Sec. II. This is a *conservative backstop estimate for preliminary design*.

Summary of guarantee status:

Result	Status	Main-text Eq.
Slope bound $N b \geq 1$	Rigorous (proved)	(23)
Scaling $N \sim \kappa L^{3/2} / \sqrt{\epsilon_{\log}}$	Heuristic (Taylor truncation + empirical κ)	(28)
Bound $E_\infty \leq L^2 / (4N) + 1 / (2b^2 N)$	Conservative heuristic	(S0.7)
N_{safe} screening depth	Conservative backstop	(S0.8)

S1. DEPTH-SCALING DERIVATION AND CONSERVATIVE SCREENING BOUND

This section provides the detailed derivations underlying the depth-scaling relations and conservative screening bounds summarized in the main text (Sec. II). These results complement the rigorous treatment in Sec. S0.

S1.1 Local expansion and exponential-like behavior

To provide immediate local intuition (without changing the global minimax objective), let $\delta = I - I_0$ around the flank-centered point $I_0 = L/2$ and impose $a + bI_0 = -1$. With the local normalization $C = 2^N$ (so that $\tilde{y}(I_0) = 1$), a third-order expansion of $\tilde{y}(I) = C[1 + (a + bI)^2]^{-N}$ gives

$$\tilde{y}(I) \approx 1 + Nb\delta + \frac{N^2}{2}b^2\delta^2 + \frac{N(N^2 - 1)}{6}b^3\delta^3 + \mathcal{O}(\delta^4), \quad (\text{S1.1})$$

so with $b \sim 1/N$, the linear and quadratic coefficients align with those of $e^\delta = 1 + \delta + \delta^2/2 + \delta^3/6 + \dots$, explaining why the initialization is already close before refinement.

S1.2 Log-domain analysis and scaling derivation

For depth scaling, the logarithmic domain is more transparent. Under the same flank centering ($a + bI_0 = -1$), expand around $I_0 = L/2$ with $\delta = I - I_0$ to obtain

$$\ln \tilde{y}(I) = \text{const} + Nb\delta + \frac{Nb^3}{6}\delta^3 + \mathcal{O}(\delta^4). \quad (\text{S1.2})$$

At $a + bI_0 = -1$, the quadratic term cancels identically in the log expansion; imposing slope matching ($Nb = 1$) gives

$$\ln \tilde{y}(I) = \text{const} + \delta + \frac{\delta^3}{6N^2} + \mathcal{O}(\delta^4). \quad (\text{S1.3})$$

Hence the leading log-domain residual scales as $r(\delta) \sim \delta^3/N^2$. Over $I \in [0, L]$ with $|\delta| \leq L/2$, this implies $E_\infty \sim L^3/N^2$. Requiring $E_\infty \leq \varepsilon_{\log}$ leads to

$$N \propto \frac{L^{3/2}}{\sqrt{\varepsilon_{\log}}}, \quad (\text{S1.4})$$

which explains the scaling used in the main-text engineering estimate (Eq. (28)). This derivation is heuristic (not a formal guarantee), and the prefactor remains platform- and fitting-criterion dependent.

S1.3 Conservative upper bound and screening depth

For fixed b and the identical-detuning family ($a_1 = \dots = a_N \equiv a$), one can write a conservative heuristic condition for achieving a prescribed log-tolerance. A simple normalization is to enforce $\tilde{y}(L) = 1$ (matching the target $f(L) = 1$). For a particular constructive choice of a that keeps $(a + bI)$ large and negative across $[0, L]$, one can bound the worst-case log-error as

$$E_\infty \leq \frac{L^2}{4N} + \frac{1}{2b^2N}. \quad (\text{S1.5})$$

(This is a conservative rule of thumb; obtaining a formal guarantee would require a separate proof.) As a screening estimate (not a formal guarantee), one may use

$$N \geq \left\lceil \frac{L^2/4 + 1/(2b^2)}{\ln(1 + \varepsilon)} \right\rceil. \quad (\text{S1.6})$$

While this bound is typically pessimistic, it provides a conservative backstop-style estimate for preliminary design screening. The rigorous derivation of these bounds, including the concavity conditions and slope-matching assumptions, is given in Sec. S0.3.

S2. WORKED EXAMPLE AND EMPIRICAL LOGIT-RANGE CALIBRATION

This section provides the detailed worked example for the input-to-output mapping and the empirical logit-range calibration tables referenced in the main text (Sec. III).

S2.1 Worked input-to-output mapping example

As a worked example, consider

$$x = [-3.2, 1.2, 4.8, -0.9]. \quad (\text{S2.1})$$

Compute $m = \max x_n = 4.8$. Then $u = x - m = [-8.0, -3.6, 0, -5.7]$ and $L = -\min u_n = 8.0$. The mapped control-signal levels are

$$I = u + L = [0, 4.4, 8.0, 2.3], \quad (\text{S2.2})$$

and the required normalized exponentials are $e^{x_n - m} = e^{u_n} = e^{I_n - L}$. Using the fitted model directly,

$$T_k(I_n) = \frac{1}{1 + (a_k + bI_n)^2}, \quad y(I_n) = \prod_{k=1}^N T_k(I_n).$$

Under the identical-detuning fit ($a_1 = \dots = a_N \equiv a$), this becomes

$$\tilde{y}(I_n) = C y(I_n) = C \left[\frac{1}{1 + (a + bI_n)^2} \right]^N.$$

For the re-fitted parameters used in this example,

$$\begin{aligned} a &= -1.4588, & b &= 0.10202, \\ N &= 10, & C &= 3.0896 \times 10^1. \end{aligned} \quad (\text{S2.3})$$

which gives

$$\begin{aligned} \tilde{y}(I_n) &= C \left[\frac{1}{1 + (a + bI_n)^2} \right]^N, \\ &\approx [3.44 \times 10^{-4}, 2.73 \times 10^{-2}, \\ &\quad 9.74 \times 10^{-1}, 3.26 \times 10^{-3}]. \end{aligned} \quad (\text{S2.4})$$

For reference, the corresponding target terms are

$$I_n - L = [-8.0, -3.6, 0, -5.7], \quad (\text{S2.5})$$

and

$$\begin{aligned} [e^{I_n - L}] &\approx [3.35 \times 10^{-4}, 2.73 \times 10^{-2}, \\ &\quad 1.00, 3.35 \times 10^{-3}]. \end{aligned} \quad (\text{S2.6})$$

S2.2 Effective-range percentiles and clipping calibration

We first estimate the logit range observed in data and then choose clipping accordingly. From two autoregressive Transformers (distilgpt2 and gpt2) and two public corpora (Tiny Shakespeare and *Pride and Prejudice*) [1–5] at context length 128, the effective range

$$L_{\text{eff},\alpha} = \max(\log p_{\text{kept}}) - \min(\log p_{\text{kept}}), \quad \alpha = 0.999, \quad (\text{S2.7})$$

fell in a relatively narrow band, summarized in Table S2.

TABLE S1: Example ($N = 10$): approximating $e^{x_n - m} = e^{I_n - L}$ using $\tilde{y}(I) = C[1 + (a + bI)^2]^{-N}$ with parameters re-fitted on $I \in [0, 8.0]$ using the same minimax pipeline.

x_n	I_n	target $e^{x_n - m}$	approx $\tilde{y}(I_n)$	rel. err.
-3.2	0.0	3.3546×10^{-4}	3.4443×10^{-4}	2.673%
1.2	4.4	2.7324×10^{-2}	2.7325×10^{-2}	0.004%
4.8	8.0	1.0000	0.9739	2.608%
-0.9	2.3	3.3460×10^{-3}	3.2585×10^{-3}	2.614%

TABLE S2: Effective-range percentiles ($L_{\text{eff},0.999}$) at context length 128.

Percentile	All runs (4 runs)	GPT-2
p50	6.92–7.23	7.09–7.23
p90	8.60–8.75	8.73–8.75
p95	8.97–9.12	9.06–9.12
p99	9.50–9.69	9.58–9.69

We then test clipping on the same rows with

$$E_{\text{cum}}(t) = \frac{1}{2} \|\text{softmax}(u^{(t)}) - \text{softmax}(u)\|_1, \quad (S2.8)$$

$$u^{(t)} = \max(u, t), \quad u = s - \max(s).$$

and require $\text{p99}\{E_{\text{cum}}\} \leq 10^{-3}$ (0.1% budget). This criterion is satisfied at $t = -12$ ($\text{p99} \approx 4.27 \times 10^{-4}$) and violated at $t = -11$ ($\text{p99} \approx 1.24 \times 10^{-3}$), so we set $t^* = -12$ ($N_{\text{clip}} = 12$).

In practice, we (i) estimate an effective L from data, (ii) verify that fixed clipping keeps softmax error small, and (iii) choose representative design points (e.g., $L \approx 8$ or $L \approx 12$) while treating the clipped tail as negligible. Full protocol details, clipping-sweep tables/plots, and per-run statistics are provided in Sec. S3.

S2.3 Illustrative synthetic range map

As a design-space reference, we consider synthetic logit-range regimes using $L = \max(x) - \min(x)$ after $QK^\top / \sqrt{d_k}$ scaling. These regimes are illustrative rather than corpus-level percentiles; using the same fitting pipeline, Table S3 summarizes achievable approximation error versus depth.

TABLE S3: Synthetic softmax logit-range regimes ($L = \max(x) - \min(x)$) and fitted worst-case relative error (design-space illustration; not intended as corpus-level statistics).

L regime	$N = 5$	$N = 10$	$N = 20$	$N = 30$
$L = 8$	10.9%	2.68%	0.67%	0.30%
$L = 12$	40.0%	9.25%	2.27%	1.01%
$L = 16$	113%	23.0%	5.44%	2.41%

Table S3 suggests a simple rule of thumb: the required depth depends mainly on the target L regime. Near $L \approx 8$, moderate depth reaches a few-percent error, whereas $L \gtrsim 12$ typically requires deeper cascades to approach $< 1\%$ error.

We include Table S3 as a synthetic design map rather than an empirical benchmark.

S3. EMPIRICAL LOGIT-RANGE EXTRACTION FROM REAL TRANSFORMER RUNS

We extracted empirical attention-logit ranges from real model runs to complement the synthetic L -regime map in the main text. We used two open-source autoregressive Transformers (distilgpt2 and gpt2) and two public corpora (Tiny Shakespeare and *Pride and Prejudice*), with context length 128 and causal masking. For each valid attention row, if $p = \text{softmax}(s)$ then the raw range is

$$L_{\text{raw}} = \max(s) - \min(s) = \max(\log p) - \min(\log p), \quad (35)$$

where \max/\min are taken over valid causal keys only. Because very small tail probabilities can dominate $\min(\log p)$, we additionally report an effective range:

$$L_{\text{eff},\alpha} = \max(\log p_{\text{kept}}) - \min(\log p_{\text{kept}}), \quad (36)$$

where keys are sorted by attention weight and retained until cumulative mass reaches $\alpha = 0.999$.

To stay within a 16 GB RAM budget, we processed one model at a time, batch size 1, fixed windowing (stride 128), and streaming histogram quantiles. Observed process RSS stayed below 1.24 GB in these runs.

TABLE S4: Empirical global logit-range percentiles from real model-dataset runs (context length 128): raw vs effective ($\alpha = 0.999$).

Model	Dataset	raw p95	raw p99	L_{eff} p50	L_{eff} p90	L_{eff} p95	L_{eff} p99
distilgpt2	tiny_shakespeare	22.82	69.00	7.10	8.60	8.97	9.50
distilgpt2	pride_prejudice	21.76	68.60	6.92	8.60	9.03	9.57
gpt2	tiny_shakespeare	25.48	43.34	7.23	8.73	9.06	9.58
gpt2	pride_prejudice	24.13	40.92	7.09	8.75	9.12	9.69

For quick linkage to the main manuscript: the effective-range summary quoted in the main text corresponds to this table (all runs: p50 = 6.92–7.23, p90 = 8.60–8.75, p95 = 8.97–9.12, p99 = 9.50–9.69), and the GPT-2 subset is p50 = 7.09–7.23, p90 = 8.73–8.75, p95 = 9.06–9.12, p99 = 9.58–9.69.

Clipping-validity sweep (additional justification). To test whether practical clipping magnitudes can be used without materially changing softmax outputs, we evaluated a thresholded-logit approximation. For each row, define $u = s - \max(s)$ and, for threshold $t \leq 0$,

$$u^{(t)} = \max(u, t), \quad p^{(t)} = \text{softmax}(u^{(t)}). \quad (37)$$

We report the cumulative softmax error

$$E_{\text{cum}}(t) = \frac{1}{2} \left\| p^{(t)} - p \right\|_1, \quad (38)$$

then sweep $t \in \{-14, -13, \dots, -6\}$ and compute p50/p90/p95/p99 of E_{cum} over all extracted rows.

TABLE S5: Global clipping-validity sweep: percentile statistics of $E_{\text{cum}}(t)$ versus clipping threshold t .

t	p50	p90	p95	p99
-14	2.53×10^{-5}	4.55×10^{-5}	4.80×10^{-5}	5.18×10^{-5}
-13	2.69×10^{-5}	4.85×10^{-5}	7.38×10^{-5}	1.48×10^{-4}
-12	2.99×10^{-5}	1.21×10^{-4}	2.13×10^{-4}	4.27×10^{-4}
-11	3.31×10^{-5}	3.95×10^{-4}	6.55×10^{-4}	1.24×10^{-3}
-10	3.72×10^{-5}	1.28×10^{-3}	2.01×10^{-3}	3.58×10^{-3}
-9	4.41×10^{-5}	4.04×10^{-3}	6.11×10^{-3}	1.03×10^{-2}
-8	2.25×10^{-4}	1.26×10^{-2}	1.83×10^{-2}	2.91×10^{-2}
-7	2.76×10^{-3}	3.85×10^{-2}	5.30×10^{-2}	7.89×10^{-2}
-6	1.88×10^{-2}	1.11×10^{-1}	1.43×10^{-1}	1.95×10^{-1}

Under a conservative budget criterion $\text{p99}\{E_{\text{cum}}\} \leq 10^{-3}$, the least negative admissible threshold in this sweep is $t^* = -12$ ($\text{p99} \approx 4.27 \times 10^{-4}$). Equivalently, the operational clipping magnitude is $N_{\text{clip}} \equiv -t^* = 12$. Notably, this is closely aligned with the empirical effective-range scale (Table S4: p99 of $L_{\text{eff},0.999}$ up to ≈ 9.69), indicating that clipping-constrained implementation and effective-range statistics operate in the same order-of-magnitude range budget. This supports using a practical clipping magnitude comparable to the design range scale ($L \approx N_{\text{clip}}$) while keeping aggregate softmax distortion below 0.1%.

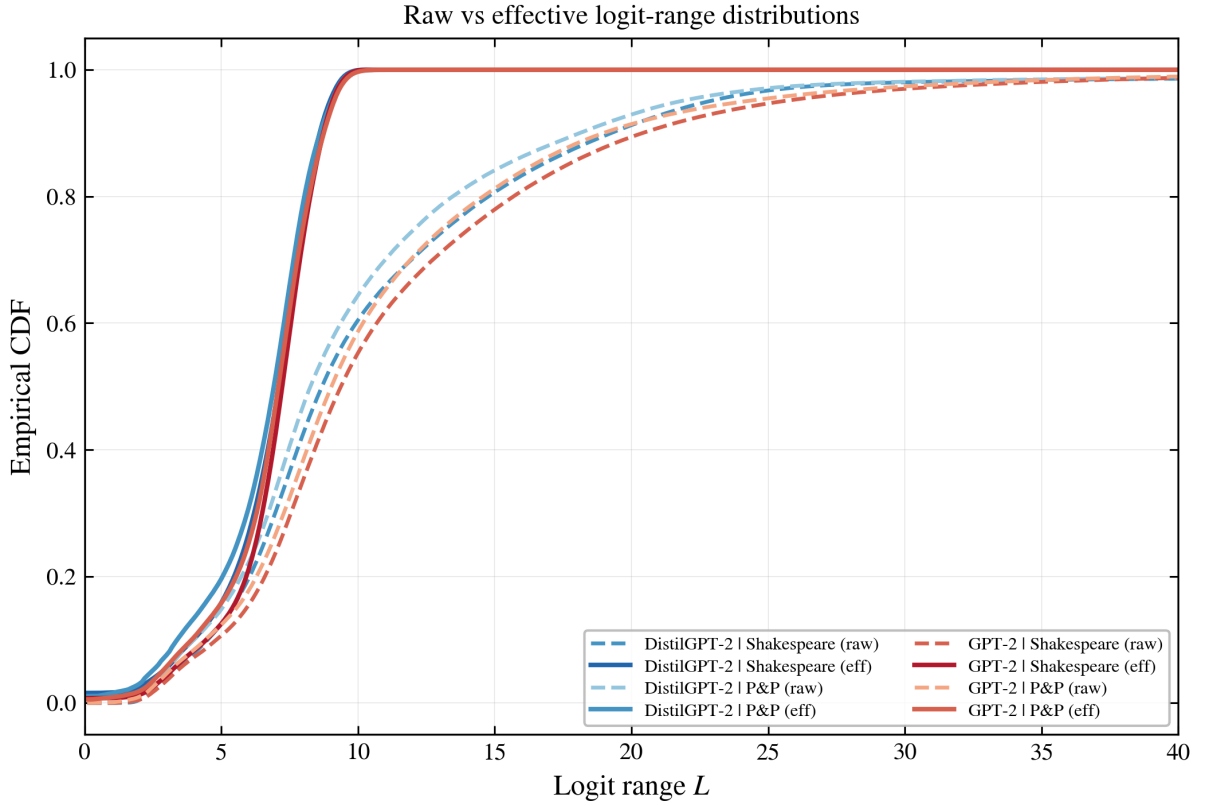


FIG. S1: Global CDFs of raw L_{raw} (dashed) and effective $L_{\text{eff},0.999}$ (solid) for the four model–dataset runs.

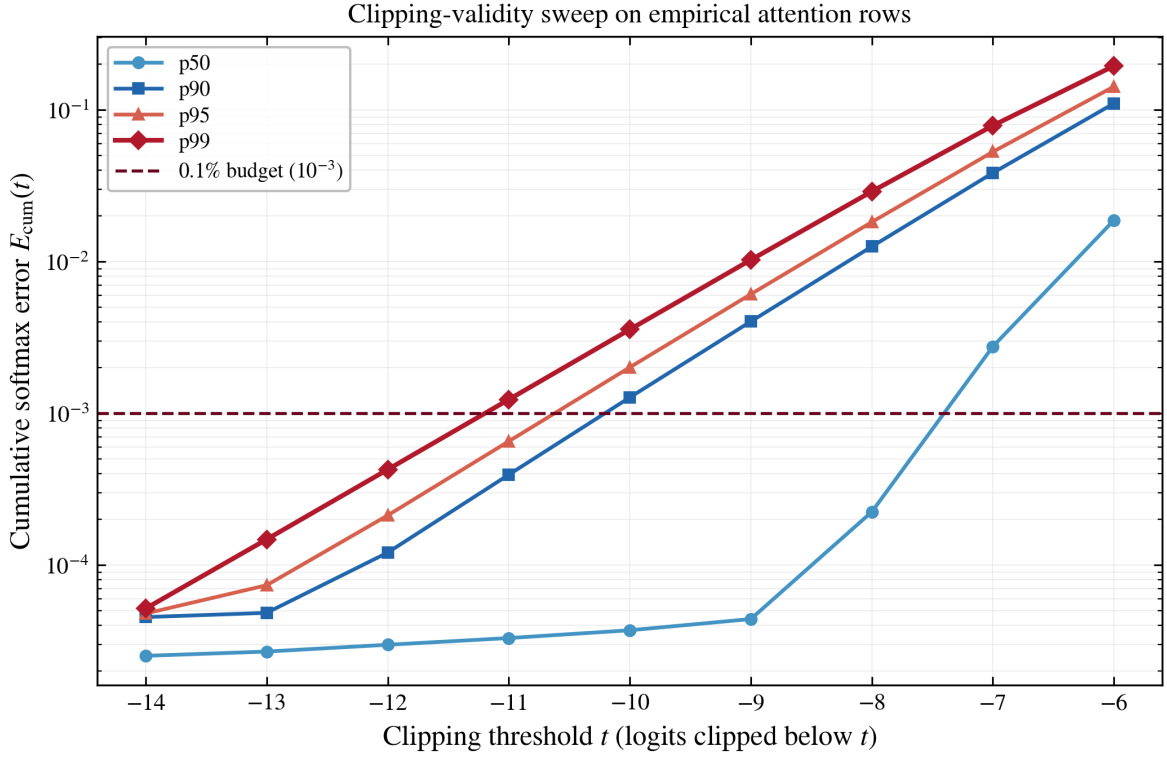


FIG. S2: Percentile curves of cumulative softmax error $E_{\text{cum}}(t)$ versus clipping threshold t . The dashed line marks the 0.1% budget (10^{-3}).

S4. FDTD METHODOLOGY DETAILS AND X-CUT b_V DERIVATION

This section provides the detailed FDTD simulation methodology, the step-by-step X-cut arc electrode voltage sensitivity derivation, and the full cascade optimization table referenced in the main text (Sec. IV–V).

S4.1 z-refined 3-fix simulation strategy

For thin-film LiNbO₃ structures, special care is required in the vertical (z) direction due to the high index contrast between LiNbO₃ ($n_o \approx 2.21$) and SiO₂ ($n \approx 1.44$) and the sub-micron film thickness. We apply a “z-refined 3-fix” strategy:

1. **Ordinary index correction:** the material model uses the corrected ordinary refractive index n_o appropriate for the TE mode in X-cut geometry, rather than the extraordinary index n_e that governs TM propagation;
2. **z -span expansion:** the simulation z -span is extended beyond the minimal waveguide region to include sufficient substrate and superstrate so that evanescent field tails are captured without PML truncation artifacts;
3. **Auto-mesh:** accuracy level 3; conformal variant 1 meshing is enabled, and no manual mesh override is applied. The resulting vertical grid spacing in the slab region is approximately 55 nm, providing ~ 2 cells across the 100 nm slab.

This refinement strategy is critical for obtaining converged results in TFLN ring resonators, where the high- Q spectral features are sensitive to numerical dispersion in under-resolved thin films [6]. Table S6 lists the full simulation parameters.

TABLE S6: 3D FDTD simulation parameters (Lumerical).

Parameter	Value
Solver	Lumerical 3D FDTD
Mesh type	Conformal variant 1
Mesh accuracy	3 (auto-mesh)
z -mesh override	None (auto-mesh)
Simulation time	50 ps
Auto shutoff	1×10^{-6}
Wavelength range	1530 nm to 1570 nm
Grid size	$532 \times 816 \times 44$
Source	Broadband mode source (TE ₀)

S4.2 X-cut arc electrode b_V step-by-step derivation

For the X-cut circular ring with lateral S–G arc electrodes (Table II), the crystal Z-axis (c-axis) is oriented at 45° from the horizontal axis in the substrate plane. At azimuthal angle θ around the ring, the projection of the lateral electric field onto the Z-axis is proportional to $\cos(\theta - 45^\circ)$. The $\cos(\theta - 45^\circ) = 0$ boundaries fall at $\theta = 135^\circ$ and $\theta = 315^\circ$, naturally separating the bus-waveguide coupling regions from the electrode regions. Each ring carries a full semicircular arc electrode on the side opposite to its coupling points. By the substitution $\varphi = \theta - 45^\circ$, the effective EO fill factor is

$$f_{\text{EO}} = \frac{1}{2\pi} \int_{\text{semicircle}} |\cos(\theta - 45^\circ)| d\theta = \frac{1}{2\pi} \int_{-\pi/2}^{+\pi/2} \cos \varphi d\varphi = \frac{1}{2\pi} [\sin \varphi]_{-\pi/2}^{+\pi/2} = \frac{1}{\pi} \approx 0.318. \quad (\text{S4.1})$$

The 45° rotation ensures that the electrode semicircle does not overlap with the coupling points, while the fill factor integral is identical to the standard $\cos \theta$ case by the change of variable.

The lateral S–G electrodes have gap $g_{\text{el}} = 5 \mu\text{m}$, giving an effective electrode–waveguide distance $d_{\text{eff}} \approx g_{\text{el}}/2 = 2.5 \mu\text{m}$. The lateral field geometry yields an EO overlap factor $\Gamma_{\text{EO}} = 0.7$, compared to 0.5 for a vertical electrode configuration.

The refractive index change per volt in the electrode-covered section is

$$\frac{\Delta n_{\text{eff}}}{V} = -\frac{1}{2} n_e^3 r_{33} \frac{\Gamma_{\text{EO}}}{d_{\text{eff}}} = -\frac{1}{2} \times 2.138^3 \times 30.9 \times 10^{-12} \times \frac{0.7}{2.5 \times 10^{-6}} = -4.226 \times 10^{-5} \text{ V}^{-1}. \quad (\text{S4.2})$$

The corresponding resonance wavelength shift is

$$\left. \frac{d\lambda_0}{dV} \right|_{\text{straight}} = \frac{1550 \times 4.226 \times 10^{-5}}{2.30} = 28.48 \text{ pm V}^{-1}, \quad (\text{S4.3})$$

giving an intrinsic (straight-section) voltage sensitivity of

$$b_V^{\text{straight}} = \frac{2Q_L}{\lambda_0} \left. \frac{d\lambda_0}{dV} \right|_{\text{straight}} = \frac{2 \times 15,500}{1550} \times 0.02848 = 0.570 \text{ V}^{-1}. \quad (\text{S4.4})$$

However, only the arc-electrode portion of the ring circumference contributes to the round-trip phase shift. The effective voltage sensitivity is therefore

$$b_V = b_V^{\text{straight}} \times f_{\text{EO}} = 0.570 \times \frac{1}{\pi} \approx 0.182 \text{ V}^{-1}. \quad (\text{S4.5})$$

A 1 V applied voltage shifts the normalized detuning by $\Delta a \approx 0.182$. Despite the fill-factor penalty ($f_{\text{EO}} = 1/\pi \approx 0.318$), the X-cut arc design benefits from a smaller effective electrode distance (2.5 μm vs. 4 μm for vertical configurations) and a higher overlap factor (0.7 vs. 0.5), which partially compensate the reduced active length.

S4.3 Full cascade optimization table

Table S7 presents the complete optimization results for the standard dynamic range $L = 8$ (corresponding to $e^8 \approx 2981$, i.e., 34.7 dB), covering all cascade depths from $N = 5$ to $N = 30$.

TABLE S7: Cascade optimization results for $L = 8$. The bias voltage $V_{\text{bias}} = |a|/b_V$ sets the DC offset, and $V_{\text{ctrl}} = bL/b_V$ is the maximum control voltage at $I = L$. Voltages computed with $b_V = 0.182 \text{ V}^{-1}$ (FDTD-calibrated best resonance $Q_L = 15,500$).

N	a	b	E_∞	ε_{max} (%)	V_{bias} (V)	V_{ctrl} (V)
5	-2.0789	0.21658	0.1035	10.91	11.4	9.5
8	-1.5959	0.12896	0.0412	4.20	8.8	5.7
10	-1.4588	0.10202	0.0265	2.68	8.0	4.5
12	-1.3731	0.08450	0.0184	1.86	7.5	3.7
15	-1.2914	0.06726	0.0118	1.19	7.1	3.0
17	-1.2543	0.05923	0.0092	0.92	6.9	2.6
20	-1.2136	0.05025	0.0067	0.67	6.7	2.2
25	-1.1685	0.04013	0.0043	0.43	6.4	1.8
30	-1.1392	0.03341	0.0030	0.30	6.3	1.5

Key thresholds for the minimum number of rings at various error targets are:

- $\varepsilon < 10\%$: $N \geq 6$,
- $\varepsilon < 5\%$: $N \geq 8$,
- $\varepsilon < 2\%$: $N \geq 12$,
- $\varepsilon < 1\%$: $N \geq 17$,
- $\varepsilon < 0.5\%$: $N \geq 24$.

These thresholds are *independent* of the quality factor Q , since the minimax approximation operates entirely in normalized detuning space. The Q factor affects only the physical voltage required to achieve the necessary detuning range, through b_V .

S4.4 Lorentzian fit validation

Figure S3 shows the Lorentzian fit to the FDTD drop-port resonance near $\lambda = 1566 \text{ nm}$. The analytical Lorentzian $T_{\text{drop}}(\Delta\lambda) = A/[1 + (2Q\Delta\lambda/\lambda_0)^2]$ with $Q_L = 15,500$ closely tracks the FDTD data, validating the single-ring transfer function model used in the cascade analysis.

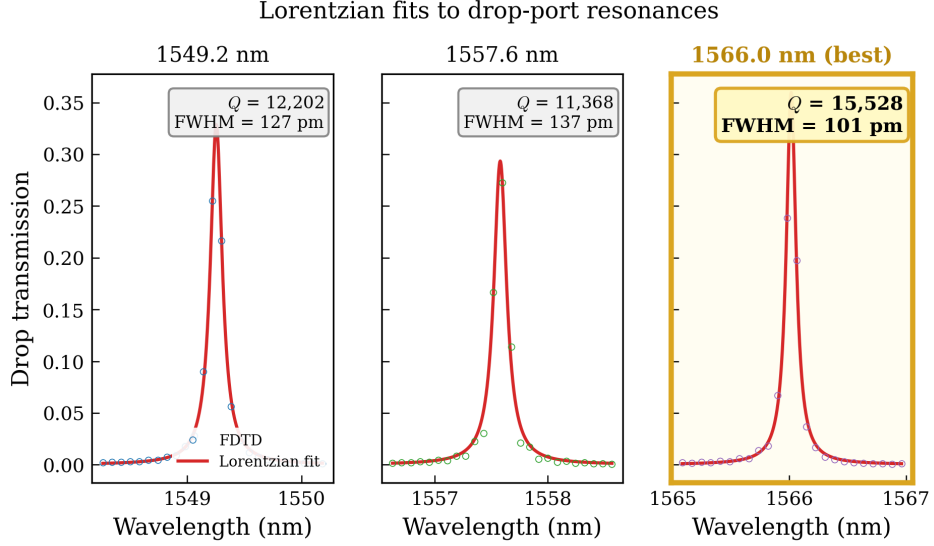


FIG. S3: Lorentzian fit to the FDTD drop-port resonance. Markers: FDTD data; solid line: Lorentzian fit. The extracted quality factor is $Q_L = 15,500$ with $\text{FWHM} = 101$ pm.

S4.5 Eigenmode (FDE) analysis of theoretical Q_i

To quantify how far below the physical limit the FDTD-extracted $Q_i = 38,800$ lies, we perform a two-dimensional finite-difference eigenmode (FDE) analysis of the bent rib waveguide cross-section using Lumerical MODE Solutions.

a. Setup. The FDE solver models the cross-section of the rib waveguide at the design bend radius $R = 20$ μm and wavelength $\lambda = 1550$ nm, with perfectly matched layer (PML) boundaries on all four edges. The geometry is identical to the 3D FDTD model: 600 nm total LiNbO_3 ($n_o = 2.211$, lossless dielectric), 100 nm slab, 500 nm rib etch, waveguide width $W = 1.4$ μm , on a 2 μm SiO_2 substrate ($n = 1.444$) with air cladding. The mesh is set to 300×300 cells over a 6 $\mu\text{m} \times 3$ μm cross-section, yielding effective grid spacings $\Delta x \approx 20$ nm and $\Delta y \approx 10$ nm—substantially finer than the 3D FDTD auto-mesh (55 nm vertical).

b. Complex effective index. The FDE solver returns a complex effective index $n_{\text{eff}} = n_r + i n_i$ for each guided mode, where the imaginary part n_i encodes propagation loss. For the fundamental TE mode at $R = 20$ μm :

$$n_{\text{eff}} = 1.9653 + i(4.73 \times 10^{-8}), \quad (39)$$

$$\alpha_{\text{rad+leak}} = \frac{4\pi n_i}{\lambda} = 0.383 \text{ m}^{-1} \quad (0.017 \text{ dB cm}^{-1}). \quad (40)$$

Since the material is set as lossless, this α captures only bending radiation loss and substrate leakage through the 100 nm slab. The corresponding quality factor is

$$Q_{\text{rad+leak}} = \frac{2\pi n_g}{\alpha_{\text{rad+leak}} \lambda} = 2.43 \times 10^7, \quad (41)$$

where $n_g = 2.354$ is the group index from the FDE solver (consistent with the FDTD FSR-derived $n_g = 2.30$; the small difference arises from the straight-section approximation inherent to 2D FDE).

c. Decomposition into bending and leakage. A separate FDE run with $R = 1$ mm (effectively straight) yields $Q_{\text{leak}} = 2.93 \times 10^7$, isolating the substrate leakage contribution. The pure bending radiation quality factor follows from

$$\frac{1}{Q_{\text{bend}}} = \frac{1}{Q_{\text{rad+leak}}} - \frac{1}{Q_{\text{leak}}}, \quad Q_{\text{bend}} = 1.43 \times 10^8. \quad (42)$$

This confirms that bending radiation loss at $R = 20$ μm is negligible; substrate leakage through the thin slab is the dominant geometric loss channel.

d. Material absorption. The FDE mode profile yields a confinement factor $\Gamma = 0.887$ (fraction of the optical intensity within the LiNbO_3 core and slab regions). The material-absorption-limited quality factor is

$$Q_{\text{abs}} = \frac{2\pi n_g}{\Gamma \alpha_{\text{mat}} \lambda}, \quad (43)$$

where α_{mat} is the bulk material power-attenuation coefficient of LiNbO_3 at 1550 nm. Table S8 evaluates Eq. (43) for representative TFLN absorption values from the literature [6, 7].

TABLE S8: Theoretical intrinsic quality factor Q_i of the $R = 20 \mu\text{m}$ TFLN ring, decomposed into radiation (Q_{bend}), substrate leakage (Q_{leak}), and material absorption (Q_{abs}). Sidewall scattering (fabrication-dependent) is excluded. The total is $1/Q_i = 1/Q_{\text{rad+leak}} + 1/Q_{\text{abs}}$ with $Q_{\text{rad+leak}} = 2.43 \times 10^7$.

Material condition	α_{mat} (dB/cm)	Q_{abs}	Q_i (total)
Bulk LiNbO_3 (pristine)	0.002	2.3×10^8	2.2×10^7
High-quality TFLN	0.01	4.7×10^7	1.6×10^7
Good TFLN	0.03	1.6×10^7	9.5×10^6
Typical TFLN	0.1	4.7×10^6	3.9×10^6

For high-quality TFLN ($\alpha_{\text{mat}} \lesssim 0.01 \text{ dB cm}^{-1}$), the theoretical Q_i exceeds 10^7 —more than $400\times$ higher than the FDTD-extracted value of 38,800. This confirms that the FDTD result is dominated by numerical mesh artifacts (approximately two cells across the 100 nm slab), not by physical loss mechanisms. Bending radiation loss at $R = 20 \mu\text{m}$ is negligible ($Q_{\text{bend}} = 1.43 \times 10^8$); the dominant geometric loss channel in the ideal structure is substrate leakage through the thin slab ($Q_{\text{leak}} = 2.93 \times 10^7$).

S5. FABRICATED HIGH- Q DESIGN PROJECTIONS

Reproducing $Q_i > 10^5$ in three-dimensional FDTD is computationally impractical: at accuracy level 3 the 100 nm slab requires $\Delta z \lesssim 20$ nm to suppress staircase-induced scattering, inflating wall times beyond 30 days per run. The numerically extracted $Q_i = 38,800$ therefore represents a *simulation* floor, not a physical one. A two-dimensional MODE-solver bend analysis confirms $Q_{\text{bend}} > 4.5 \times 10^7$ for $R = 20 \mu\text{m}$, placing bending radiation loss far below any realistic intrinsic loss.

Table S9 surveys recent high- Q TFLN microring demonstrations. These studies show that $Q_i \geq 9 \times 10^6$ has been demonstrated in X-cut TFLN using multiple fabrication routes, including Ar^+ milling, wet etching, and ICP-RIE/CMP-based processes.

TABLE S9: Demonstrated intrinsic quality factors in TFLN micro-ring resonators. “EO compatible” indicates whether the fabrication process preserves electrode patterning capability.

Ref.	Q_i	R (μm)	w (μm)	Etch
Zhang [8]	10^7	80	~ 2	Ar^+ mill
Gao [9]	10^8	100	~ 3	CMP*
Zhuang [10]	9×10^6	100	~ 2	Wet etch
Song [11]	2.9×10^7	200	4.5	ICP-RIE+CMP

All processes except * are EO-electrode compatible. *CMP-only (no dry etch); subsequent electrode patterning may degrade Q_i .

To project cascade performance into the fabricated regime, we fix $Q_{\text{ext}} = 25,800$ (the FDTD-extracted coupling quality factor at gap = 100 nm) and compute $D_{\text{max}} = [Q_i / (Q_i + Q_{\text{ext}})]^2$ for three representative intrinsic quality factors (Table S10).

TABLE S10: Projected cascade transmission for fabricated Q_i values at fixed $Q_{\text{ext}} = 25,800$. D_{max}^N is the ideal on-resonance cascade transmission in dB. The minimax approximation error ε_{max} depends only on N and L (not on Q_i); at $N = 20$, $L = 8$: $\varepsilon_{\text{max}} = 0.67\%$ (Table I).

Projection	Q_i	D_{max}	$N=10$	$N=20$	$N=30$
FDTD baseline	3.88×10^4	0.36	-44.3	-88.5	-132.8
Conservative	5×10^5	0.90	-4.4	-8.8	-13.2
Moderate	10^6	0.95	-2.2	-4.5	-6.7
Optimistic	5×10^6	0.99	-0.44	-0.88	-1.3

Even in the conservative scenario ($Q_i = 5 \times 10^5$), $D_{\text{max}} = 0.90$ and the $N = 10$ cascade loss is only -4.4 dB—an order-of-magnitude improvement over the FDTD baseline. The moderate projection ($Q_i = 10^6$) matches the “fabricated high- Q ” column in Table V. Because $Q_{\text{bend}} \approx 4.5 \times 10^7 \gg Q_i$ for all projections, bending loss is never the bottleneck; the dominant loss mechanism is sidewall scattering, which is determined entirely by fabrication quality. The literature values in Table S9 support the view that intrinsic quality factors in the projected range are physically achievable in TFLN—albeit with wider waveguides ($w \geq 2 \mu\text{m}$) and larger ring radii ($R \geq 80 \mu\text{m}$) than the present design. Transferring comparable sidewall quality to our geometry ($R = 20 \mu\text{m}$, $w = 1.4 \mu\text{m}$) is an open fabrication challenge; the projections in Table S10 should be read as design targets contingent on achieving it.

S6. INSERTION LOSS BUDGET DETAILS

For a cascade of N rings, the total insertion loss is modeled as

$$IL_{\text{tot}} \approx N \cdot IL_{\text{stage}} + IL_{\text{coupling}}, \quad (\text{S6.1})$$

where IL_{stage} is the per-ring insertion loss at off-resonance operation and IL_{coupling} accounts for fiber-to-chip and chip-to-fiber coupling losses. Using typical loss numbers from the literature [12–16], we consider two scenarios:

- **Optimistic:** $IL_{\text{stage}} = 0.08$ dB, $IL_{\text{coupling}} = 1.5$ dB. Then $IL_{\text{tot}} \approx 1.90$ dB ($N = 5$), 2.30 dB ($N = 10$), 3.10 dB ($N = 20$), and 3.80 dB ($N = 30$).
- **Conservative:** $IL_{\text{stage}} = 0.25$ dB, $IL_{\text{coupling}} = 3.0$ dB. Then $IL_{\text{tot}} \approx 4.25$ dB ($N = 5$), 5.50 dB ($N = 10$), 8.00 dB ($N = 20$), and 10.5 dB ($N = 30$).

In both scenarios, $N = 5$ – 10 is manageable for probe-power budgeting, whereas $N = 20$ and $N = 30$ require tighter power budgeting and more amplification margin. Higher IL_{tot} raises the required probe SNR and pushes operation closer to the detector noise floor, reducing usable dynamic range.

e. Four-component loss breakdown. The total insertion loss of the cascade has four components:

1. **On-resonance cascade transmission** D_{max}^N (dominant; see Table V);
2. **Inter-ring coupling loss** $(N - 1) \times (-10 \log_{10} \eta_{\text{coupling}})$, where η_{coupling} is the power transfer efficiency at each inter-ring bus section. Two-ring FDTD yields $\eta_{\text{coupling}} \approx 0.9$ for the present diagonal-bus geometry, corresponding to ~ 0.46 dB per inter-ring stage;
3. **Off-resonance propagation loss** $N \times IL_{\text{stage}}$, where $IL_{\text{stage}} = 0.08$ – 0.25 dB per ring [12–14, 16];
4. **Fiber-to-chip coupling loss** $IL_{\text{coupling}} = 1.5$ – 3.0 dB [15].

Table V presents the *ideal* on-resonance budget (D_{max}^N only). Including all four components for the present diagonal-bus layout: in the FDTD-characterized regime ($D_{\text{max}} = 0.36$, $N = 5$), the total loss is approximately $22.2 + 1.8 + 0.4 + 1.5 \approx 26$ dB; in the fabricated high- Q regime ($D_{\text{max}} = 0.95$, $N = 30$), the total loss is $6.7 + 13.3 + 2.4 + 1.5 \approx 24$ dB. The inter-ring coupling loss dominates in the high- Q regime, underscoring that layout optimization (e.g., adiabatic tapers or straight-bus coupling) is as important as achieving $D_{\text{max}} \geq 0.95$ through quality-factor improvement. For an optimized layout with $\eta_{\text{coupling}} \geq 0.98$ (≤ 0.09 dB per stage), the $N = 30$ total loss would reduce to ~ 13 dB.

S7. ENERGY EFFICIENCY DETAILED DERIVATION

This section provides the detailed energy-per-operation derivations for both electrical analog exponential circuits and the photonic MRR cascade, as summarized in the main text (Sec. V).

S7.1 Electrical analog exponential circuits

Three main families of electrical circuits realize the exponential function in the analog domain:

f. BJT translinear / Gilbert cell circuits. The collector current of a bipolar junction transistor is $I_C = I_S \exp(V_{BE}/V_T)$, providing an intrinsic exponential map [17, 18]. A Gilbert cell multiplier—the core building block of translinear exponential circuits—dissipates 250–325 μW in typical CMOS/BiCMOS implementations [19]. At a signal bandwidth of $B \approx 100$ MHz, the energy per operation is

$$E_{\text{Gilbert}} = \frac{P}{B} = \frac{300 \mu\text{W}}{100 \text{ MHz}} = 3 \text{ pJ}. \quad (\text{S7.1})$$

g. CMOS subthreshold exponential circuits. A MOSFET in weak inversion exhibits $I_D \propto \exp(V_{GS}/nV_T)$, enabling direct exponential computation at ultra-low power [18]. A reconfigurable softmax circuit in 180 nm CMOS implements a 10-input softmax at $V_{DD} = 500$ mV with $P = 3 \mu\text{W}$ [20]. Per-channel: $P_{\text{exp}} \approx 0.43 \mu\text{W}$. At $B \approx 1$ MHz (limited by subthreshold f_T):

$$E_{\text{sub-}V_T} = \frac{0.43 \mu\text{W}}{1 \text{ MHz}} = 0.43 \text{ pJ}. \quad (\text{S7.2})$$

This is the most energy-efficient electrical approach, but at severely limited bandwidth (~ 1 MHz).

h. Digital CMOS (for reference). A digital exponential via Taylor series requires ~ 10 multiply-add operations. Using Horowitz’s energy figures [21] for 45 nm at 0.9 V: 32-bit FP multiply costs 3.7 pJ, FP add costs 0.9 pJ, giving

$$E_{\text{digital}} \approx 10 \times (3.7 \text{ pJ} + 0.9 \text{ pJ}) = 46 \text{ pJ}. \quad (\text{S7.3})$$

At 8-bit precision (sufficient for inference): ~ 2.3 pJ.

S7.2 Photonic MRR cascade: single-channel energy derivation

We evaluate the energy at $N = 30$ cascaded X-cut TFLN micro-ring resonators with $R = 20 \mu\text{m}$ in the fabricated high- Q regime ($Q_i = 10^6$, $Q_L \approx 25,200$; Supplementary Sec. S5), which achieves $\varepsilon_{\text{max}} = 0.30\%$ with $V_{\text{ctrl}} = 0.91$ V (fully CMOS-compatible). The energy per exponential operation has three components:

(i) Electro-optic tuning energy. Each ring is tuned by charging the arc electrode capacitance to V_{ctrl} . For the lateral S–G arc electrodes covering one semicircle ($L_{\text{arc}} = \pi R = 62.8 \mu\text{m}$), the electrode capacitance is estimated as

$$C_{\text{el}} \approx 18 \text{ fF}, \quad (\text{S7.4})$$

based on coplanar electrode modeling for TFLN lateral S–G geometries with $g_{\text{el}} = 5 \mu\text{m}$ (comparable to values reported by Bahadori *et al.* [22] for similar geometries). The switching energy per ring at $V_{\text{ctrl}} = 0.91$ V (using the projected $Q_L = 25,200$, which gives $b_V = 0.295 \text{ V}^{-1}$):

$$E_{\text{ring}} = \frac{1}{2} C_{\text{el}} V_{\text{ctrl}}^2 = \frac{1}{2} \times 18 \text{ fF} \times (0.91 \text{ V})^2 = 7.4 \text{ fJ}. \quad (\text{S7.5})$$

For $N = 30$ rings: $E_{\text{EO}} = 30 \times 7.4 = 0.22$ pJ.

Note the important scaling: $E_{\text{EO}} \propto 1/N$ since $b \propto 1/N$ from minimax optimization, because

$$E_{\text{EO}} \propto N \times V_{\text{ctrl}}^2 \propto N \times (b/b_V)^2 \propto 1/N. \quad (\text{S7.6})$$

The bias voltage (3.9 V) is static and does not contribute per-operation energy.

(ii) Laser source energy (amortized). Because every cascade channel uses the same fixed probe wavelength, a single CW laser can be shared among M parallel softmax channels via a $1 \times M$ optical power splitter. With wall-plug efficiency $\eta_{\text{WPE}} \approx 15\%$ [23], the per-channel optical power is $P_{\text{opt}} = P_{\text{in}}/M \approx 100 \mu\text{W}$ (for $P_{\text{in}} = 1$ mW, $M = 10$), requiring $P_{\text{laser}} \approx 667 \mu\text{W}$ per channel. At $f_{\text{mod}} = 10$ GHz: $E_{\text{laser}} = 667 \mu\text{W} / 10 \text{ GHz} = 67$ fJ.

(iii) Photodetector energy. Integrated SiGe photodetectors with TIA achieve sub-pJ reception [24]: $E_{\text{PD}} \approx 0.5$ pJ.

The total single-channel energy is

$$E_{\text{photonic}}^{(\text{1ch})} = E_{\text{EO}} + E_{\text{laser}} + E_{\text{PD}} = 0.22 + 0.07 + 0.50 = 0.79 \text{ pJ}. \quad (\text{S7.7})$$

S7.3 Q -factor scaling of energy efficiency

Since $V_{\text{ctrl}} \propto 1/Q$ and $E_{\text{EO}} \propto V_{\text{ctrl}}^2$, the EO energy scales as $1/Q^2$. Table S11 shows the total energy for $N = 30$ at various quality factors.

TABLE S11: Energy per exponential operation vs. quality factor ($N = 30$, $\varepsilon_{\text{max}} = 0.30\%$, X-cut arc electrode with b_V scales linearly with Q ; $C_{\text{el}} = 18$ fF). $E_{\text{laser}} + E_{\text{PD}} = 0.57$ pJ is the Q -independent floor. The dagger (†) marks the FDTD-calibrated quality factor; the double dagger (‡) marks the high- Q design point ($Q_i = 10^6$). Excludes thermal stabilization (0.15–0.60 pJ for $N = 30$).

Q	V_{ctrl} (V)	V_{bias} (V)	E_{EO} (pJ)	E_{total} (pJ)
5,000	4.57	19.5	5.64	6.21
10,000	2.28	9.7	1.40	1.97
12,500	1.83	7.8	0.90	1.47
15,500 [†]	1.47	6.3	0.58	1.15
20,000	1.14	4.9	0.35	0.92
25,200 [‡]	0.91	3.9	0.22	0.79
30,000	0.76	3.2	0.16	0.73
50,000	0.46	1.9	0.06	0.63

At $Q_L = 15,500$ (FDTD-calibrated), the EO contribution (0.58 pJ) is comparable to the optical floor, placing the design in the efficient operating regime. Beyond $Q \approx 30,000$, the EO contribution becomes negligible and the total energy saturates near the floor; further Q improvement primarily benefits CMOS driver voltage compatibility rather than energy.

i. Additional energy contributions. The estimates above exclude two further contributions: (i) DAC energy for setting the per-ring control voltages, typically 0.1–1 pJ per conversion at 10 GHz bandwidth; and (ii) thermal stabilization power for maintaining resonance alignment, estimated at ~ 50 – 200 μW per ring for TFLN (lower than silicon due to the small thermo-optic coefficient of LiNbO_3 , $dn/dT \approx 3.9 \times 10^{-6} \text{ K}^{-1}$). At 10 GHz modulation rate, the thermal contribution amounts to ~ 0.005 – 0.02 pJ per ring per operation. For the $N = 30$ cascade, this sums to 0.15–0.60 pJ, which is comparable to E_{EO} and must be included in the total: $E_{\text{total}} \approx 0.94$ – 1.39 pJ. The total energy comparison should therefore be treated as an order-of-magnitude estimate.

S7.4 Comparison with electronic implementations

Here we provide an order-of-magnitude energy comparison between electrical analog exponential circuits and our photonic MRR cascade, grounding the analysis in published device data and first-principles estimates. We assume a shared CW laser with total optical output $P_{\text{in,tot}} = 1$ mW, split across $M = 10$ parallel softmax channels via a $1 \times M$ power splitter, yielding per-channel input $P_{\text{in,ch}} = 100$ μW . The output power at the cascade drop port is $P_{\text{out}} = P_{\text{in,ch}} \times D_{\text{max}}^N$, which ranges from 0.61 μW (FDTD regime, $N = 5$) to 21.5 μW (fabricated regime, $N = 30$) (Table V).

j. Electrical analog exponential circuits. Three main families of electrical analog exponential circuits are compared: BJT translinear/Gilbert cell (~ 3 pJ at 100 MHz [17–19]), CMOS subthreshold (~ 0.43 pJ at 1 MHz [18, 20]), and digital FP32 Taylor series (~ 46 pJ at 1 GHz [21]).

k. Photonic MRR cascade: single-channel energy. For $N = 30$ X-cut TFLN micro-ring resonators in the self-consistent high- Q regime ($Q_L = 25,200$), the three energy components are EO tuning ($E_{\text{EO}} = 0.22$ pJ), amortized laser ($E_{\text{laser}} = 0.07$ pJ, shared across $M = 10$ parallel channels), and photodetector ($E_{\text{PD}} = 0.50$ pJ), yielding $E_{\text{photonic}} = 0.79$ pJ. Including thermal stabilization for $N = 30$ rings (0.15–0.60 pJ), the total rises to 0.94–1.39 pJ. Notably, $E_{\text{EO}} \propto 1/N$ since $b \propto 1/N$ from minimax optimization.

l. Single-channel comparison. Table S12 presents the comparison. The photonic cascade at $N = 30$ achieves 0.79 pJ baseline— $3.8\times$ lower than the BJT Gilbert cell (3 pJ) and $58\times$ lower than digital FP32 (46 pJ). Including thermal stabilization (0.94–1.39 pJ), the advantage over INT8 (2.3 pJ) is 1.7–2.4 \times , while operating at 10 GHz bandwidth. At fabricated $Q \geq 30,000$, E_{EO} drops to 0.16 pJ and $E_{\text{total}} \approx 0.73$ pJ (excluding thermal; Table S11), recovering a 3.2 \times advantage over INT8. Subthreshold CMOS achieves the lowest energy (0.43 pJ) but at 10,000 \times lower bandwidth.

m. Caveats. These values are order-of-magnitude estimates, not device-accurate predictions. The photonic estimate excludes DAC energy for voltage generation (typically 0.1–1 pJ per conversion at 10 GHz bandwidth, shared with any analog approach) and thermal tuning power for maintaining resonance alignment (~ 50 – 200 μW per ring for

TABLE S12: Energy per exponential operation: single-channel comparison.

Implementation	E/op (pJ)	Bandwidth	Notes
Digital FP32 (Taylor)	~ 46	1 GHz	10 FP MACs
BJT Gilbert cell	~ 3	100 MHz	Analog
Digital INT8 (Taylor)	~ 2.3	1 GHz	10 INT MACs
Photonic MRR ($N=30$)	0.94–1.39	10 GHz	Analog [†]
Subthreshold CMOS	~ 0.43	1 MHz	Analog

[†]0.79 pJ excluding thermal; 0.94–1.39 pJ including thermal. Self-consistent with fabricated high- Q regime ($Q_L = 25,200$); see Supplementary Sec. S7.

TFLN, lower than silicon due to the small thermo-optic coefficient of LiNbO_3 , $dn/dT \approx 3.9 \times 10^{-6} \text{ K}^{-1}$). Effective precision at the photodetector is limited to ~ 6 – 8 bits by shot noise and receiver electronics. The energy advantage over electrical implementations is strongest in the fabricated high- Q regime ($D_{\max} \geq 0.95$), where $N = 30$ is practical and V_{ctrl} remains CMOS-compatible.

S8. MONTE CARLO ROBUSTNESS UNDER DEVICE NON-IDEALITIES

This section describes the robustness model summarized in the main text. For the fitted $L = 8$, $N = 10$ design ($a = -1.4588$, $b = 0.10202$), each Monte Carlo chip sample includes: (i) per-ring static detuning spread, (ii) per-ring sensitivity spread, (iii) global thermal drift and crosstalk-like slope drift, (iv) stage insertion-loss variation, (v) control-channel noise, and (vi) detector noise with one-point calibration at $I = L$.

For ring k , we use

$$T_k(I) = \frac{1}{1 + (a_k + b_k I + d_{\text{th}} + d_{\text{xt}} I/L)^2}, \quad (44)$$

with

$$y(I) = \prod_{k=1}^N T_k(I) \times 10^{-IL_{\text{tot}}/10}, \quad (45)$$

and one-point calibration $\tilde{y}(I) = C_{\text{cal}} y(I)$ such that $\tilde{y}(L) = 1$ for the same chip instance.

TABLE S13: Non-ideality distributions used in the Monte Carlo sweeps.

Parameter	Nominal	Stress
σ_a	0.020	0.032
$\sigma_{b,\text{rel}}$	0.020	0.032
σ_{th}	0.015	0.025
σ_{xt}	0.012	0.020
σ_I	0.004	0.007
IL_{stage} (dB, $\mu \pm \sigma$)	0.12 ± 0.03	0.18 ± 0.05
σ_{det}	3.0×10^{-6}	6.0×10^{-6}

TABLE S14: Monte Carlo summary (same run reported in main text).

Metric	Nominal	Stress
Median $\text{KL}(p_{\text{ref}} \ p_{\text{approx}})$	2.17×10^{-4}	7.39×10^{-4}
p95 $\text{KL}(p_{\text{ref}} \ p_{\text{approx}})$	5.92×10^{-4}	2.21×10^{-3}
Median max $ \Delta p $	0.170%	0.193%
p95 max $ \Delta p $	0.319%	0.419%

Conservative-bound sketch used for the main-text screening equation. For the identical-detuning family with fixed b , define

$$\ln \tilde{y}(I) = N \phi(a + bI) - N \phi(a + bL), \quad \phi(u) = -\ln(1 + u^2), \quad (46)$$

so that $\tilde{y}(L) = 1$ by construction. Around a constructive choice with $a + bI < 0$ on $[0, L]$, a second-order remainder argument for the mismatch between the target slope and the fitted slope yields a term scaling as $L^2/(4N)$, while the flank-curvature penalty contributes a term scaling as $1/(2b^2N)$. Combining the two contributions gives the screening inequality

$$E_{\infty} \lesssim \frac{L^2}{4N} + \frac{1}{2b^2N}, \quad (47)$$

which leads to the conservative screening equation reported in the main manuscript. We emphasize that this is a conservative heuristic design rule (not a formal minimax theorem), used only for preliminary depth screening.

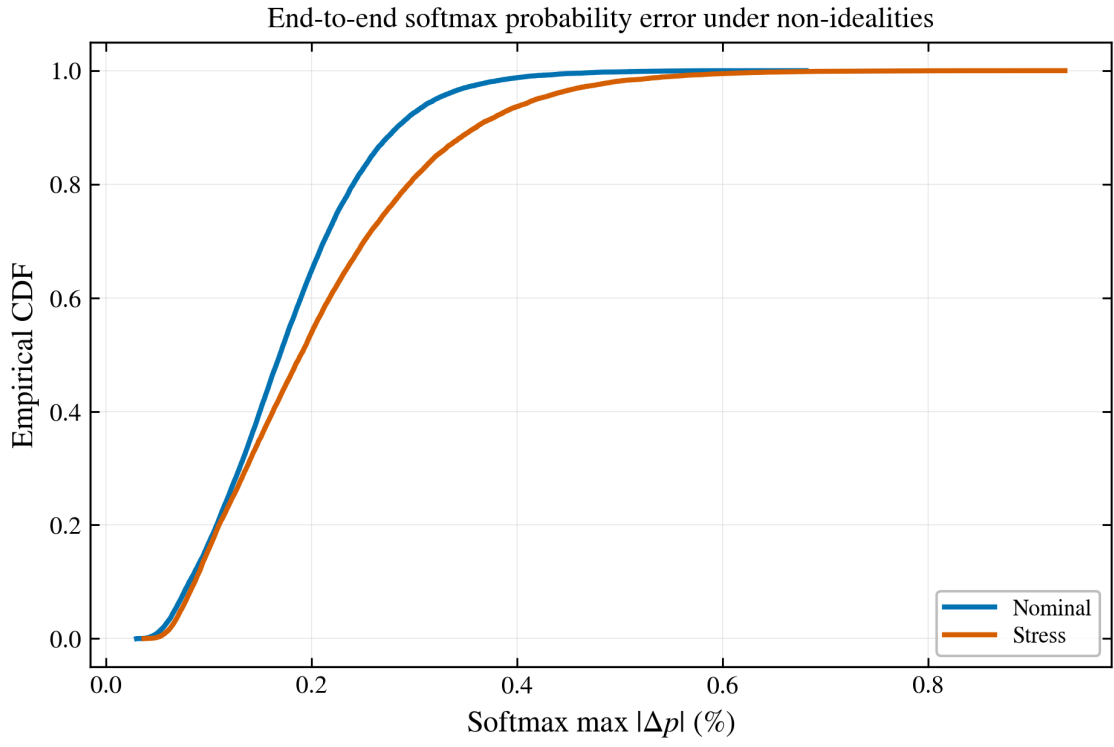


FIG. S4: CDF of end-to-end softmax probability error under the same non-ideality samples.

S9. DELAY-AWARE FEEDBACK NORMALIZATION VALIDATION

We model global normalization as a delayed PI-controlled loop:

$$S(t) = G(t)P(t) + n(t), \quad (48)$$

$$\tau \frac{dP}{dt} = -P(t) + u(t - T_d), \quad (49)$$

$$u(t) = K_p e(t) + K_i \int e(t) dt, \quad e(t) = S_{\text{ref}} - S(t), \quad (50)$$

with actuator saturation $0 \leq u \leq P_{\text{max}}$. A piecewise $G(t)$ profile is used to emulate workload changes. For physical intuition, Table S15 converts normalized delay/settling metrics into absolute-time examples.

TABLE S15: Example absolute-time interpretation of normalized PI-loop metrics using one representative stable case $((K_p, K_i, T_d/\tau) = (0.55, 0.8, 0.2))$ and a $\pm 2\%$ settling-time definition ($T_{\text{settle}} \sim 12.4\tau$).

Assumed τ	Delay $T_d = 0.2\tau$	Settling $\sim 12.4\tau$	Interpretation
100 ns	20 ns	1.24 μs	fast loop
1 μs	200 ns	12.4 μs	moderate loop
5 μs	1 μs	62 μs	slower loop

Reference-backed latency context for bottleneck screening. To place the delayed-loop times against mixed-signal system latencies, Table S16 summarizes representative time scales with explicit path classes (on-chip vs off-chip) for memory and interconnect paths, alongside conversion latency ranges. These are intentionally order-of-magnitude ranges (not fixed constants), and can shift with architecture, clocking, and protocol stack choices.

TABLE S16: Representative subsystem latency ranges used for conservative bottleneck screening in Sec. S9.

Subsystem path	T_{sys}	Sources
On-chip memory (L1/L2)	20–200 ns	[25]
Off-chip memory (DRAM)	200–700 ns	[25, 26]
ADC conversion	10–710 ns	[27, 28]
DAC + driver/settling	1–200 ns	[29]
On-chip interconnect (NoC)	5–100 ns	[30]
Off-chip I/O (PCIe/CXL)	1–10 μs	[25, 31]

Conservative risk-screening heuristic for loop latency. As a screening heuristic, we use the settling time from one representative stable case $((K_p, K_i, T_d/\tau) = (0.55, 0.8, 0.2))$; Table S18), with settling defined as the first time entering and remaining within a $\pm 2\%$ band around S_{ref} , as a normalization-loop latency proxy:

$$T_{\text{norm}} \approx 12.4\tau. \quad (51)$$

This value is *not* a universal bound; different gain settings, delay ratios, or loop architectures will yield different settling times. It is used only as a reference point for order-of-magnitude risk screening. Define the conservative screening metric

$$T_{\text{norm}} \geq \beta T_{\text{sys}}, \quad (52)$$

with $\beta = 1$ (high-risk screening line) and $\beta = 0.5$ (early-warning line); this is a heuristic risk indicator, not a formal dominance proof. The corresponding threshold is

$$\tau_{\text{crit}}(\beta) = \frac{\beta T_{\text{sys}}}{12.4}. \quad (53)$$

Table S17 gives the resulting numeric ranges.

For the explicit examples in Table S15, $\tau = 0.1 \mu\text{s}$ gives $T_{\text{norm}} \approx 1.24 \mu\text{s}$, $\tau = 1 \mu\text{s}$ gives $T_{\text{norm}} \approx 12.4 \mu\text{s}$, and $\tau = 5 \mu\text{s}$ gives $T_{\text{norm}} \approx 62 \mu\text{s}$. These numbers indicate a risk trend (not a hard boundary): for this representative case, the normalization loop is typically non-dominant when τ is well below the relevant τ_{crit} band, and it may become dominant

TABLE S17: Computed τ_{crit} ranges from Eq. (53) using Table S16.

Subsystem	T_{sys} range	$\tau_{\text{crit}} (\beta = 0.5)$	$\tau_{\text{crit}} (\beta = 1)$
On-chip memory path	20–200 ns	0.81–8.06 ns	1.61–16.13 ns
Off-chip memory path	200–700 ns	8.06–28.23 ns	16.13–56.45 ns
ADC conversion	10–710 ns	0.40–28.63 ns	0.81–57.26 ns
DAC+driver/settling	1–200 ns	0.04–8.06 ns	0.08–16.13 ns
On-chip interconnect (NoC)	5–100 ns	0.20–4.03 ns	0.40–8.06 ns
Off-chip I/O fabric	1–10 μs	0.04–0.40 μs	0.08–0.81 μs

as τ approaches or exceeds that band. The transition depends on path class (on-chip vs off-chip) and on architecture-specific timing closure, including whether the normalization path lies on the end-to-end critical path (Table S16). **Accordingly, this analysis is intended for preliminary risk screening only; concrete implementations require full timing validation.**

TABLE S18: Representative step-response cases for the delayed PI loop (settling defined by a $\pm 2\%$ band around S_{ref}).

Case	$(K_p, K_i, T_d/\tau)$	Overshoot	Settling	Stable
Stable	(0.55, 0.8, 0.2)	25.6%	$\sim 12.4\tau$	Yes
Marginal	(0.95, 1.6, 0.45)	25.6%	$\sim 12.8\tau$	Yes
Unstable	(1.2, 2.2, 0.75)	45.1%	not settled	No

TABLE S19: Stable-region fraction from gain-map scans at each delay ratio.

T_d/τ	Stable fraction
0.0	88.1%
0.2	88.0%
0.5	72.4%
0.8	47.5%

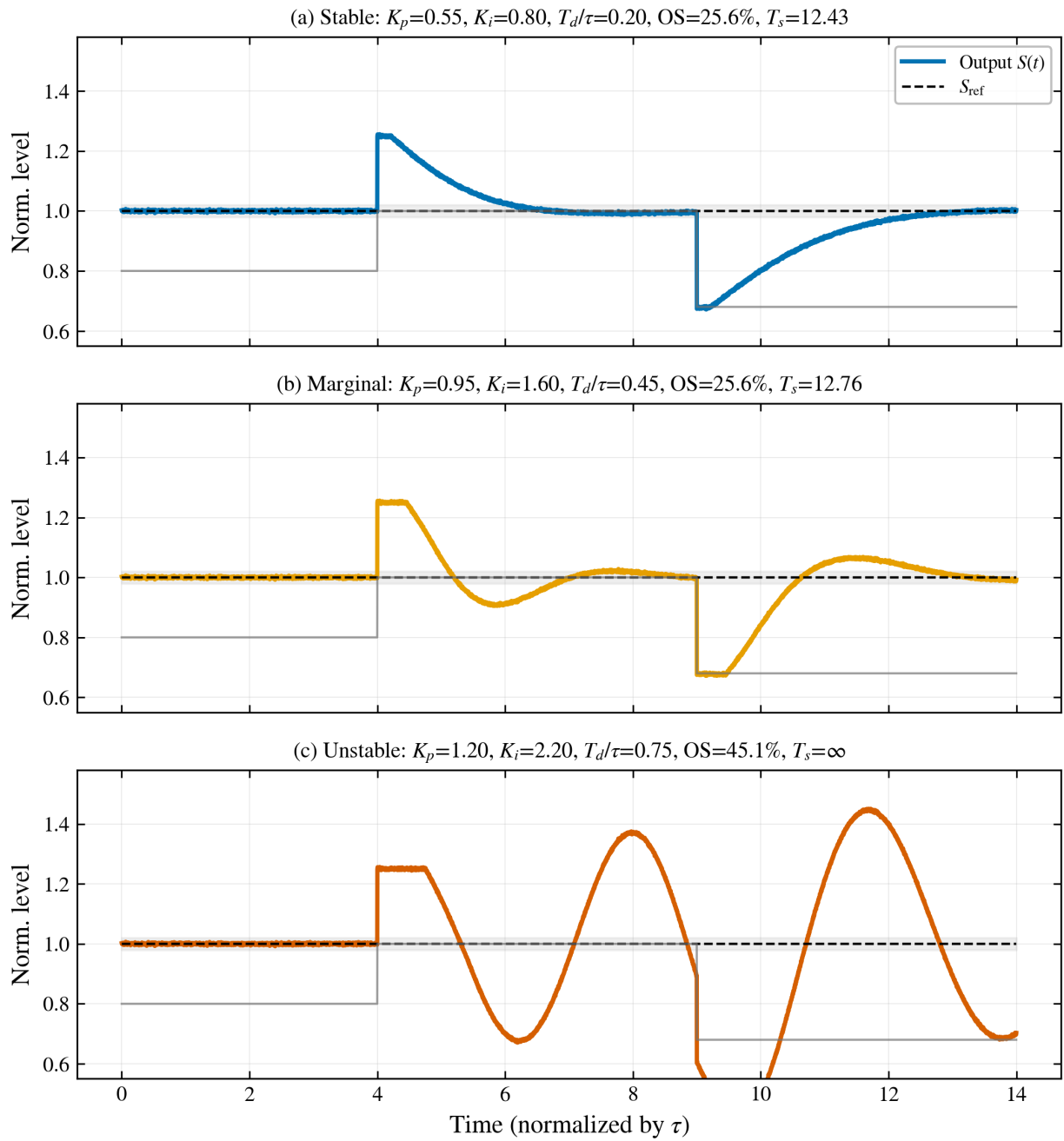


FIG. S5: Step-response examples of the delayed PI normalization loop.

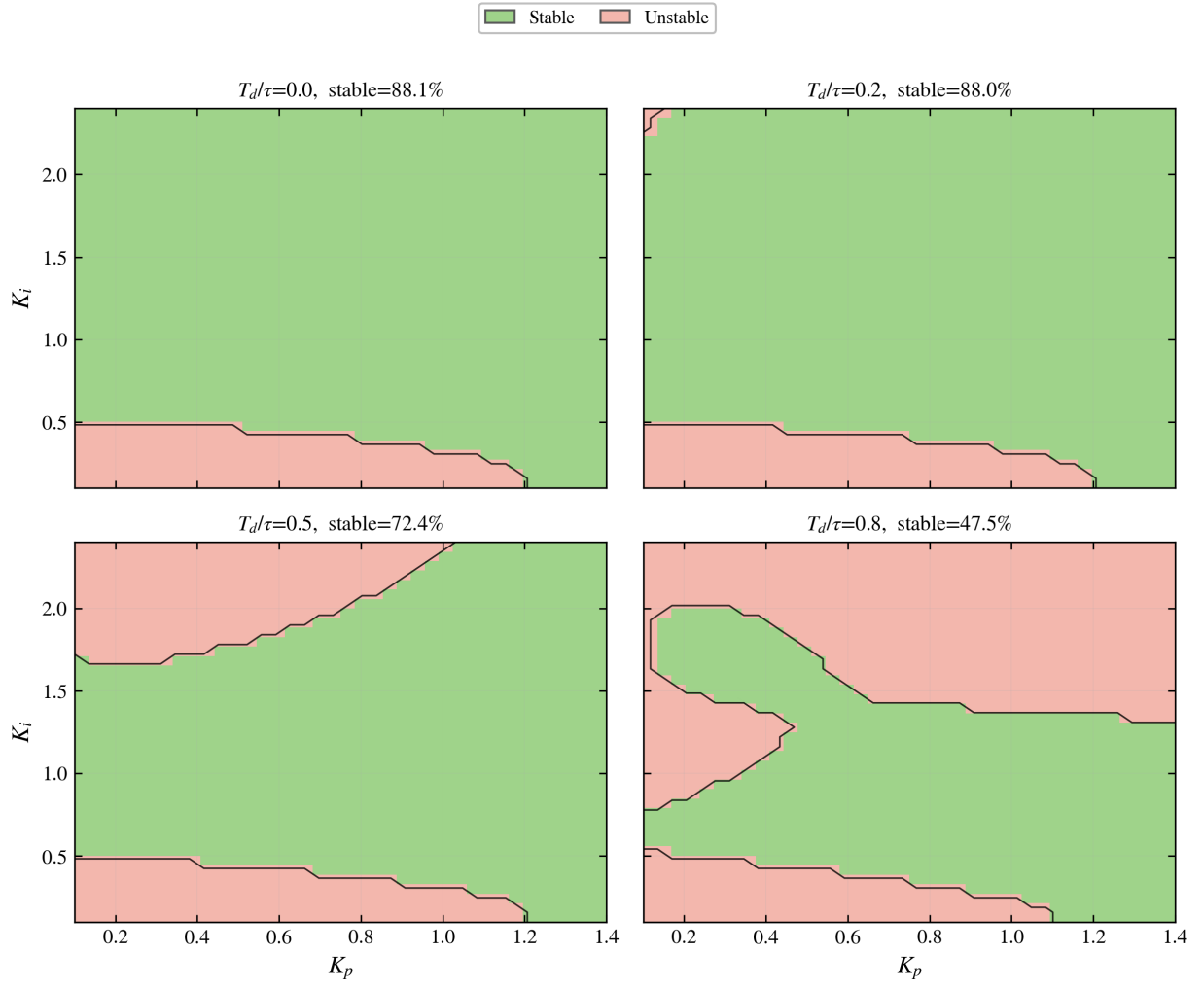


FIG. S6: Delay-dependent stability maps over scanned (K_p, K_i) ranges.

S10. REPRODUCIBILITY

Scripts used for this Supplementary validation:

- `scripts/nonideality_montecarlo.py`
- `scripts/feedback_loop_validation.py`
- `scripts/extract_logit_range_effective.py`
- `scripts/analyze_softmax_clipping_validity.py`

Public code repository: <https://github.com/hyoseokp/MRR-AEF> (commit 585e695). Empirical extraction outputs are stored under:

- `paper/empirical_L_v3/`

- [1] Ashish Vaswani, Noam Shazeer, Niki Parmar, Jakob Uszkoreit, Llion Jones, Aidan N. Gomez, Lukasz Kaiser, and Illia Polosukhin. Attention is all you need. In *Advances in Neural Information Processing Systems 30 (NeurIPS 2017)*, pages 5998–6008, 2017.
- [2] Alec Radford et al. Language models are unsupervised multitask learners. Technical report, OpenAI, 2019.
- [3] Hugging Face. distilgpt2 model card, 2025. accessed 2026-02-21.
- [4] Andrej Karpathy. Tiny shakespeare dataset (char-rnn), 2025. accessed 2026-02-21.
- [5] Jane Austen. Pride and prejudice. Project Gutenberg eBook No. 1342, 2025. accessed 2026-02-21.
- [6] Di Zhu et al. Integrated photonics on thin-film lithium niobate. *Advances in Optics and Photonics*, 13(2):242–352, 2021.
- [7] Yaowen Hu, Di Zhu, Shengyuan Lu, Xinrui Zhu, Yunxiang Song, Dylan Renaud, Daniel Assumpcao, Rebecca Cheng, CJ Xin, Matthew Yeh, Hana Warner, Xiangwen Guo, Amirhassan Shams-Ansari, David Barton, Neil Sinclair, and Marko Loncar. Integrated electro-optics on thin-film lithium niobate. *Nature Reviews Physics*, 2025.
- [8] Mian Zhang, Cheng Wang, Rebecca Cheng, Amirhassan Shams-Ansari, and Marko Loncar. Monolithic ultra-high-Q lithium niobate microring resonator. *Optica*, 4(12):1536–1537, 2017.
- [9] Renhong Gao, Ni Yao, Jianglin Guan, Li Deng, Jintian Lin, Min Wang, Lingling Qiao, Wei Fang, and Ya Cheng. Lithium niobate microring with ultra-high Q factor above 10^8 . *Chin. Opt. Lett.*, 20(1):011902, 2022.
- [10] Rongjin Zhuang, Jinze He, Yifan Qi, and Yang Li. High-Q thin-film lithium niobate microrings fabricated with wet etching. *Adv. Mater.*, 35(3):2208113, 2023.
- [11] Xinrui Zhu, Yaowen Hu, Shengyuan Lu, Hana K. Warner, Xudong Li, Yunxiang Song, Leticia S. Magalhães, Amirhassan Shams-Ansari, Neil Sinclair, and Marko Loncar. Twenty-nine million intrinsic Q-factor monolithic microresonators on thin-film lithium niobate. *Photon. Res.*, 12(8):A63–A68, 2024.
- [12] Sudip Shekhar, Wim Bogaerts, Lukas Chrostowski, John E. Bowers, Michael Hochberg, Richard Soref, and Bhavin J. Shastri. Roadmapping the next generation of silicon photonics. *Nature Communications*, 15:751, 2024.
- [13] Xaveer Leijtens et al. Multimode silicon photonics. *Nanophotonics*, 7:1571–1580, 2018.
- [14] Haoqian Li et al. In-memory photonic dot-product engine with electrically programmable weight banks. *Nature Communications*, 14:2389, 2023.
- [15] Daan Vermeulen et al. High-efficiency fiber-to-chip grating couplers realized using an advanced cmos-compatible silicon-on-insulator platform. *Optics Express*, 18(17):18278–18283, 2010.
- [16] F. S. Tan, D. J. W. Klunder, H. F. Bulthuis, G. Sengo, H. J. W. M. Hoekstra, and A. Driessen. Direct measurement of the on-chip insertion loss of high finesse microring resonators in $\text{si}_3\text{n}_4\text{-sio}_2$ technology. In *Proceedings of the IEEE LEOS Benelux Chapter*, 2001.
- [17] B. Gilbert. Translinear circuits: a proposed classification. *Electron. Lett.*, 11(1):14–16, 1975.
- [18] C. Mead. *Analog VLSI and Neural Systems*. Addison-Wesley, 1989.
- [19] B. Razavi. *Design of Analog CMOS Integrated Circuits*. McGraw-Hill, 2 edition, 2017.
- [20] J. Oh, G. Kim, and M. Je. A 0.5-v $3\text{-}\mu\text{w}$ cmos analog softmax circuit for neural-network inference. *IEEE Trans. Circuits Syst. II*, 68(5):1564–1568, 2021.
- [21] M. Horowitz. 1.1 computing’s energy problem (and what we can do about it). In *2014 IEEE International Solid-State Circuits Conference (ISSCC)*, pages 10–14, 2014.
- [22] Meisam Bahadori, Yansong Yang, Ahmed E. Hassanien, Lynford L. Goddard, and Songbin Gong. Ultra-efficient and fully isotropic monolithic microring modulators in a thin-film lithium niobate photonics platform. *Optics Express*, 28(20):29644–29661, 2020.
- [23] A. Biberman and K. Bergman. Optical interconnection networks for high-performance computing systems. *Rep. Prog. Phys.*, 75(4):046402, 2012.
- [24] D. A. B. Miller. Attojoule optoelectronics for low-energy information processing and communications. *J. Lightwave Technol.*, 35(3):346–396, 2017.

- [25] Zhe Jia, Marco Maggioni, Benjamin Staiger, and Daniele P. Scarpazza. Dissecting the NVIDIA volta GPU architecture via microbenchmarking. *arXiv preprint arXiv:1804.06826*, 2018.
- [26] Yoongu Kim, Vivek Seshadri, Donghyuk Lee, Jamie Liu, and Onur Mutlu. A case for exploiting subarray-level parallelism (SALP) in DRAM. In *Proceedings of the 39th Annual International Symposium on Computer Architecture (ISCA)*, pages 368–379, 2012.
- [27] Texas Instruments. ADC12DJ3200: 6.4-GSPS single-channel or 3.2-GSPS dual-channel, 12-bit, RF-sampling analog-to-digital converter. Datasheet (SLVSD97A, revised April 2020), 2020. Accessed 2026-02-22.
- [28] Texas Instruments. ADS8881: 18-bit, 1-MSPS, low-power, true-differential SAR ADC. Datasheet (SBAS547D, revised August 2015), 2015. Accessed 2026-02-22.
- [29] Texas Instruments. DAC38RF82/DAC38RF89: Dual-channel, 14-bit, 9-GSPS and 6-GSPS RF DACs. Datasheet (SLASEA6D, revised June 2020), 2020. Accessed 2026-02-22.
- [30] W. J. Dally and B. Towles. Route packets, not wires: on-chip interconnection networks. In *Proceedings of the 38th Design Automation Conference (DAC)*, pages 684–689, 2001.
- [31] Shintaro Sano, Yosuke Bando, Kazuhiro Hiwada, Hirotsugu Kajihara, Tomoya Suzuki, Yu Nakanishi, Daisuke Taki, and Akiyuki Kaneko. Gpu graph processing on CXL-based microsecond-latency external memory. In *Proceedings of the SC '23 Workshops of the International Conference for High Performance Computing, Networking, Storage and Analysis*, 2023.